Metal-Assisted Chemical Etching for the Direct Synthesis of Bimetallic Cu-Pd Nanoparticles on Silicon

E. Torralba, Sylvain Le Gall, Harsh Chaliyawala, Éric Chopard, Zouhir Ait Rahhou, D. Muller-Bouvet, C. Cachet-Vivier, Stéphane Bastide

Metal-Assisted Chemical Etching for the Direct Synthesis of Bimetallic Cu-Pd Nanoparticles on Silicon

Encarnación Torralba[1*], Sylvain Le Gall[2], Harsh Chaliyawala[1], Éric Chopard[1], Zouhir Ait Rahhou[1], Diane Muller-Bouvet[1], Christine Cachet-Vivier[1], Stéphane Bastide[1*]

[1] Univ Paris Est Creteil, CNRS, ICMPE, UMR 7182, 2 rue Henri Dunant, 94320 Thiais, France

[2] Laboratoire de Génie Electrique et Electronique de Paris (GeePs), UMR 8507, Université Paris-Saclay, CNRS, CentraleSupélec, Sorbonne Université, 91192 Gif sur Yvette CEDEX, France

***** Corresponding authors

E-mails: encarnacion.torralba-penalver@cnrs.fr, stephane.bastide@cnrs.fr

Abstract

An original study is presented for the synthesis of $Cu_{100-x}Pd_x$ nanoparticles directly on silicon by Metal Assisted Chemical Etching (MACE). CuPd is chosen as a representative bimetallic system on account of its interest and potential applications in catalysis and electrocatalysis, among others. The proposed methodology allows precise control of the nanoparticle bimetallic composition and structure. Thus, we demonstrate that $Cu_{100-x}Pd_x$ solid solutions and phase-separated nanoparticles can be synthesized at will by simply changing the deposition conditions. In-depth physical characterization of the synthesized material (structure, morphology, composition, oxidation state and d-band center position) is carried out by XRD, SEM-EDX and XPS. Finally, band bending simulations at the nanoscale in combination with electrochemical measurements help to interpret some of the peculiarities of the Pd, Cu and Cu_xPd_{100-x} deposits. The new method can be easily implemented, used for various silicon substrate geometries and extended to any bimetallic system whose metals are suitable for MACE of silicon.

Keywords

Silicon, Metallization, Bimetallic nanoparticles, Band bending modeling, Mixed potential theory, d-band center position

1 INTRODUCTION

Electroless metal deposition on Silicon (Si) in HF media is a well-known process based on a localized galvanic displacement reaction. It was first encountered and studied in the context of Si microelectronics processes, where metal clusters were found to be deposited in HF treatment baths due to traces of metal cations [1,2]. It was then discovered that Ag deposition in $AgNO_3$-HF solutions could be used to form Si nanowires [3], a method widely used since then. The direct synthesis of monometallic nanoparticles (NPs) on Si surfaces is now very common [4], often employed as a first step for Metal Assisted Chemical Etching (MACE) of Si in HF + Oxidizing Agent solutions [5,6]. MACE is a well-established scalable method based on metal catalysts (Pt, Ag, Cu, Au, etc. [7,8]) for nano- and micro-structuring of Si without masking or lithography steps.

To describe it briefly, the reduction of a given metal cation (M^{n+}) leading to its deposition as M^0, is coupled to the dissolution of nearby Si atoms, as long as the redox potential of M^{n+}/M is more positive than the (onset) potential for the Si electrochemical dissolution in HF (*e.g.* for Pt, Pd, Au, Ag and Cu). The redox reactions involved in the case of a divalent metal cation (as used in this study) are as follows:

$$\text{Cathodic sites:} \quad M^{2+}(l) + 2e^- \longrightarrow M(s) \qquad \text{Eq. 1}$$

$$\text{Anodic sites:} \quad Si(s) + 4HF_2^-(l) \longrightarrow SiF_6^{2-}(l) + 2e^- + 2HF + H_2(g) \qquad \text{Eq. 2}$$

with one H_2 molecule being produced, and one M atom deposited per Si atom dissolved. The global reaction is:

$$Si(s) + M^{2+}(l) + 4HF_2^-(l) \longrightarrow SiF_6^{2-}(l) + M(s) + 2HF + H_2(g) \qquad \text{Eq. 3}$$

The driving force is the redox potential difference of the two half-cells involved, *i.e.* $E^0_{cell} = E^0_1 - E^0_2$, where E^0_2 is for SiF_6^{2-}/Si (-1.24 V *vs.* SHE) [9], and E^0_1 is for the redox couple M^{2+}/M.

Si/metal NPs elements are being studied for numerous applications in microelectronics, photovoltaics, photo/electrocatalysis, sensing, etc. In the case of photo/electrocatalysis, bimetallic systems, rather than monometals, are currently more heavily researched due to their better performance in terms of selectivity and efficiency. The possibility of depositing them on Si by MACE would offer several advantages, since it is a low-cost, scalable and easy-to-implement technique, which also provides an optimal Si/metal contact free of Si surface oxides (due to the HF media). Surprisingly, despite these advantages over more complicated and costly synthesis methods, bimetallic deposition by MACE has not yet been exploited.

The literature reports a limited number of works in this area. In the specific case of bimetallic deposition by MACE of Si in aqueous HF solution, Ensafi et al. synthesized

graphene/bimetallic Si nanostructures with Pt-M (M: Pd, Ru, Rh) as electrocatalysts for HER, from mixtures of metal salts in 1% HF solutions. Only one concentration and deposition time for each system was investigated [10]. There are also a number of reports on bimetallic deposition by MACE of Si in organic media with a small amount of HF (*e.g.* DMSO + 1 wt% HF). For example, Shepida et al. showed that they could obtain PtPd nanoparticles with 3 different compositions ($Pt_{59}Pd_{41}$, $Pt_{63}Pd_{37}$, $Pt_{84}Pd_{16}$) depending on the Pt and Pd salt concentrations (4:4, 4:2, 4:1 mmol L^{-1}:mmol L^{-1}, respectively) in the deposition bath [11]. Metzler et al. studied the sequential or simultaneous deposition of Au and Pt or Pd on Si in an aqueous acid solution without HF, as catalysts for light-induced HER [12]. In this case, a Si oxide layer is formed on the surface during deposition, and no specific control of the bimetallic compositions was attempted. Subsequently, various methods based partly on MACE and partly on galvanic displacement have been proposed. For example, Chen et al. synthesized bimetallic AgM nanostructures (where M = Pt, Pd, Au) for surface-enhanced Raman scattering. They used a sequential method, first depositing Ag by MACE, then displacing galvanically Ag by Pt, Pd or Au [13]. In light of this literature, it appears that the simultaneous deposition of two metals by MACE has never been studied for its own sake, with the aim of controlling the structural and electronic properties of bimetallics in a wide range of compositions and considering the mechanisms at play when more than one metal cation is involved.

The Cu-Pd system has been the focus of much research in recent years. It has the ability to form a variety of crystalline structures (solid solution, intermetallic and phase separated), which have applications in catalysis, electrocatalysis and biosensing (e.g. water purification, glucose detection, CO_2 reduction, etc.) [14–19]. We have recently demonstrated the interest of CuPd nanoparticulated powders to increase the resistance to CO-poisoning for the electrochemical reduction of CO_2 [19]. Considering the advantages of MACE [5,20,21], its application to the transfer of the Cu-Pd system to Si pho/electrodes seemed very interesting.

The peculiarities of the electroless deposition of Pd or Cu alone on Si in HF solutions have been studied. Yae *et al.* [4] have classified these metals into two groups, which differ in their nucleation and nucleus growth behavior: (i) the platinum group, including Pt, Rh and Pd, which exhibits relatively low NP densities (regardless of the deposition time) and a progressive nucleation mode; (ii) the copper group, including Cu, Ag and Au, which exhibits high NP densities (increasing with the deposition time) and an instantaneous nucleation mode. In the first group, the initial nucleus is formed at the expense of the closely surrounding Si atoms. It grows into a NP up to a certain size where the formation of new nuclei is favored. These characteristics have been associated with the formation of a porous Si layer just below the NP,

which eventually prevents efficient hole transfer [7,22]. The second group exhibits a much higher level of nucleation activity (*e.g.* faster kinetics), with small NPs forming and being continuously dissolved by metal ions. This second group is reported to be less sensitive to the presence of Si oxide on the surface [4]. Finally, large NPs are formed by coalescence of the smaller NPs.

Since the electroless deposition of bimetallics has not yet been studied, we have carried out a study to test it and to characterize the bimetallic deposits obtained from a compositional, structural and morphological point of view (particle size, coverage rate), while also reporting on the modifications of the surface morphology caused by Si dissolution. We have tried to determine to what extent it is possible to control these different parameters in order to precisely tailor the desired bimetallic catalysts. In addition, XPS has been used to investigate whether the electronic effects influencing the catalytic properties (d-band center) depend on the composition of the bimetal and the deposition parameters. Finally, based on the experimental results and band bending simulations at the micro- and nanoscale, we have tried to explain the mechanisms and peculiarities of the deposition of bimetallic compounds of Cu and Pd, two metals that, when alone, deposit on Si in very different ways.

2 EXPERIMENTAL

Materials. The substrates were P-type boron doped (100) c-Si polished wafers, with a resistivity of 1-3 ohm·cm, and a thickness of 350-450 µm, purchased from Łukasiewicz - ITME.

Reagents. 30 wt% H_2O_2, 96-97 wt% H_2SO_4, 40 wt% HF, 65 wt% HNO_3 and absolute EtOH, all from VWR chemicals, were used as received for Si cleaning. $Pd(NO_3)_2$ (40 wt% Pd), $PdCl_2$ (59 wt%) and $Cu(SO_4)\cdot 5H_2O$ (98 wt% Cu), respectively from Merck and Acros Organics, were chosen as precursors for the electroless metallization. Dilution and cleaning were performed with 18.2 Mohm·cm ultra-pure water (Millipore).

Pre-treatment of Si. Si wafers were cleaved into 1x1 cm^2 pieces and cleaned for 20 min in piranha solution (3:1 v/v H_2SO_4/H_2O_2) to eliminate organic residues. After copious rinsing with ultra-pure water, the samples were immersed for 5 min in HF 1 mol L^{-1} to remove surface oxides and get a hydrogen passivation.

Si metallization. Cu, Pd and $Cu_{100-x}Pd_x$ NPs were deposited on clean Si supports by electroless metal deposition in HF media. Two variations were used: (1) *simultaneous deposition*, by immersion of Si in a HF solution (1.5 mol L^{-1}), containing the two metal precursors at selected concentrations according to the targeted atomic composition (*cf.* Fig. 1);

(2) *sequential deposition*, by immersion of Si, first in a HF-$CuSO_4$ solution (1.5 mol L^{-1} and 1 mmol L^{-1}, respectively), and second in a HF-Pd^{2+} solution (1.5 mol L^{-1} and 1 mmol L^{-1}, respectively), including a thorough rinsing between the two solutions (*cf.* Fig. 4). After metal deposition the samples were rinsed 3 times with ultra-pure water and dried under N_2 flux. The experiments were performed at nominal room temperature (RT) conditions (T~20-25°C), except for those related to the influence of the Pd counterion (section 3.1.1), which were carried out at 21.0°C (± 1°C) with a thermostatic water bath.

All characterizations were performed immediately after sample preparation. Samples were stored under primary vacuum if required. The 1.5 mol L^{-1} in HF provides a pH equal to 1 [8], which is required to meet the solubility of $Pd(NO_3)_2$ and $PdCl_2$ in aqueous media. The metal precursor solutions were sonicated 10 min before each deposition to ensure full solubilization.

For XRD characterization, the metallization was performed on a Si powder instead of monocrystalline Si samples, and the concentrations of metal precursors were multiplied by ten to match the higher surface area (necessary to reach an acceptable background noise-to-signal ratio, see below). Si powder was obtained by grinding monocrystalline Si samples by hand in a mortar. After metallization, the obtained powder was collected by decantation, washed 5 times with ultra-pure water and 5 times with absolute ethanol, and dried under primary vacuum.

Instrumentation and software. Scanning electron microscopy (SEM) and Energy Dispersive X-ray Spectroscopy (EDS) were performed with a Merlin FEG microscope from Zeiss equipped with AZtec system (EDS Advanced, HKL Advanced Nordlys Nano, Oxford Instruments) operating at an acceleration voltage of 10 kV. The average diameter and coverage of the NPs on the Si surfaces were determined by image processing using ImageJ software.

Structural characterization was carried out by X-Ray diffraction (XRD) using a D8 advanced Bruker diffractometer (copper K α-radiation). The software EVA and CellRef were used for XRD data processing. The metallization was performed on Si powders rather than on Si wafers as mentioned above. The larger surface area of the powders allows the X-Ray beam to interact with more deposited metal, increasing the intensity of the corresponding diffraction peaks. The concentration of the metal precursors was increased tenfold to accommodate this larger amount of deposited metal. Figure S3 int the Supporting Information (SI) shows representative SEM images of the synthesized powders.

The surface composition, oxidation state and valence band center were determined by X-ray Photoelectron Spectroscopy (XPS) on a thermo VG Scientific ESCALAB 250 system fitted with a microfocused, monochromatic Al Kα X-ray source (hυ = 1486.6 eV; spot size 650 µm, power = 15 kV x 200 W). All XPS spectra were calibrated with the C1s peak. Additionally, a

Shirley-type background was employe to correct the valence band spectra for the d-band center determinations. Additional details are given in the SI. Origin software was used for data treatment.

3 RESULTS AND DISCUSSION

3.1 Morphology and bulk composition of the bimetallic NPs

3.1.1 Simultaneous deposition

Morphology. Si samples were metallized by immersion in 1.5 mol L^{-1} HF solutions containing the copper salt, the palladium salt, or a mixture of both, with the following molar fractions: Cu^{2+}/Pd^{2+} (100/0), (25/75), (50/50), (75/25) and (0/100). The aim was to obtain deposits with different Cu-Pd compositions. Figure 1 shows SEM images in plan-view of metallized Si samples for the different metal cation fractions and three deposition times: 1, 5 and 20 min. Figure 2 shows higher magnification images together with cross section views of Si samples metallized for 20 min in solutions containing Pd^{2+}, Cu^{2+} and Cu^{2+}/Pd^{2+} (50/50).

With single-cation solutions and 1 min deposition, Pd and Cu appear as quasi-spherical NPs. Pd NPs are large (diameter ~ 60 nm) and isolated, while Cu NPs are small (diameter ~ 20 nm) and highly dispersed, resulting in surface coverage of about 6 and 30 %, respectively. The development of dendrites with increasing deposition time indicates that Pd NPs grow by reduction of Pd^{2+} on the already formed NPs (see also Figure 2 – Pd^{2+}, 20 min). On the other hand, increasing the deposition time with Cu leads to an increase of the surface coverage, followed by a coalescence of the NPs and finally a volume growth. These characteristics are in agreement with those already described in the literature (*cf.* Introduction).

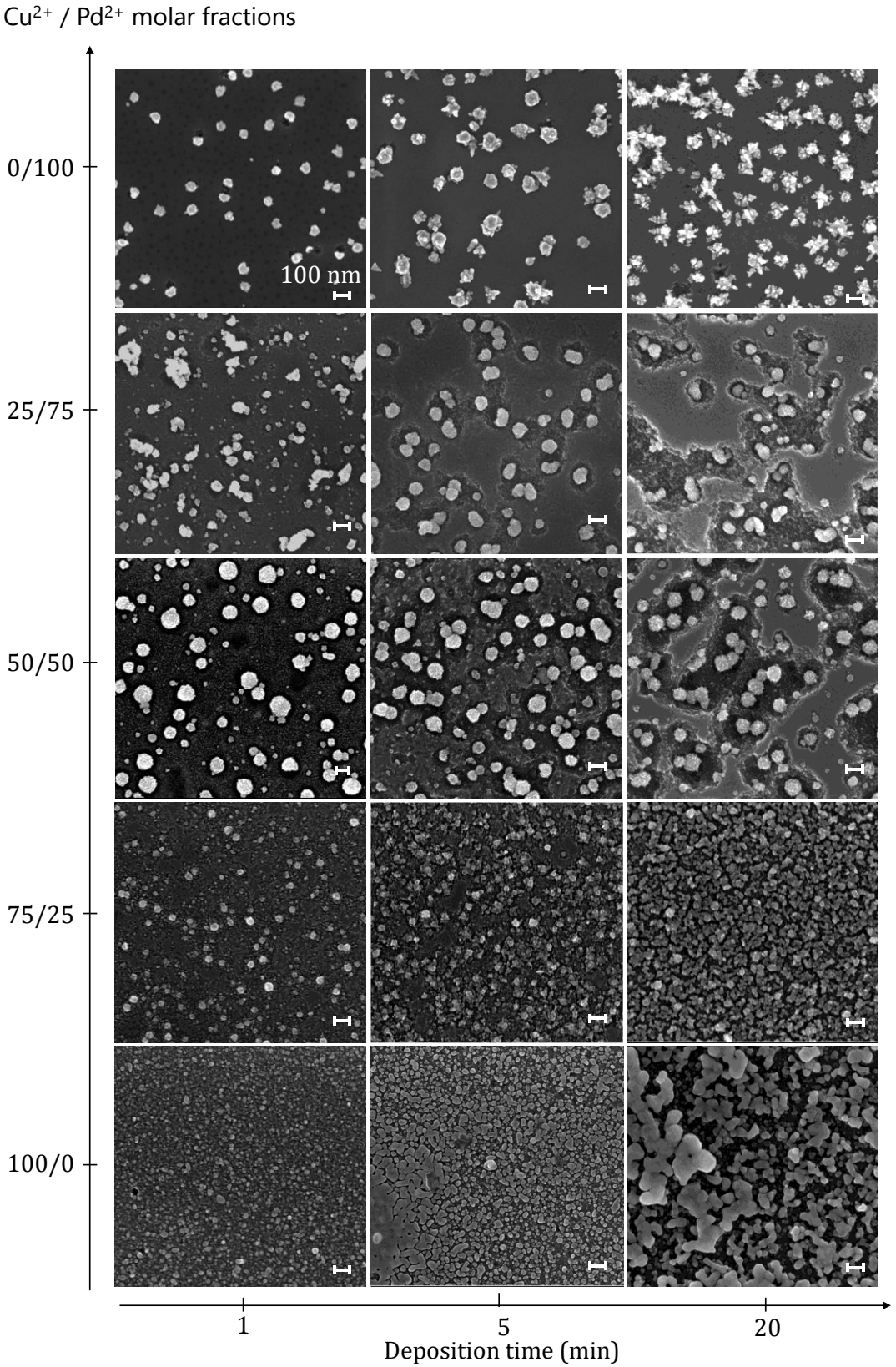

Figure 1. SEM images of Si samples metallized for 1, 5 and 20 min, by simultaneous deposition in 1.5 mol L^{-1} HF with $CuSO_4$ and $Pd(NO_3)_2$ in the following molar fractions: 0.75 and 0.25 mmol L^{-1} (75/25), 1 and 1 mmol L^{-1} (50/50), 0.25 and 0.75 mmol L^{-1} (25/75), 1 mmol L^{-1} (100/0) and (0/100). Scale bar: 100 nm.

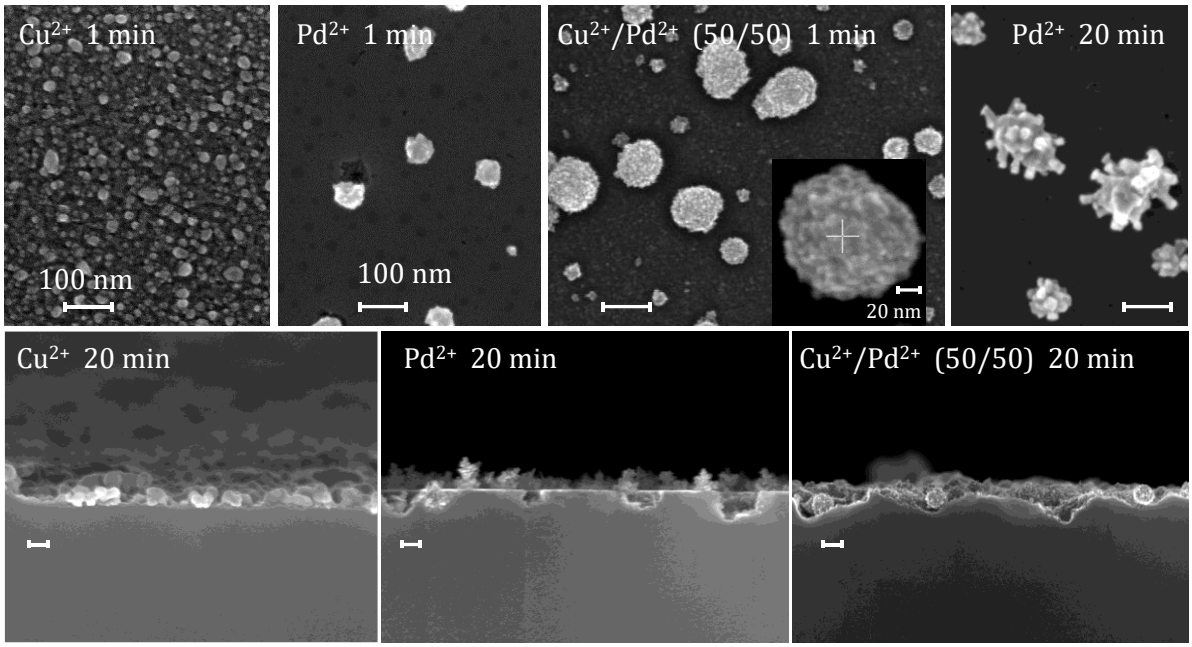

Figure 2. SEM images of Si samples metallized with $CuSO_4$ and $Pd(NO_3)_2$. Top – Plan-views showing: Cu NPs deposited for 1 min; the imprint of Si by Pd NPs after 1 min deposition; the granular morphology of $Cu_{50}Pd_{50}$ NPs obtained by simultaneous deposition (50/50, 1 min); the dendritic morphology of Pd NPs after 20 min deposition. Bottom – Cross-section views showing: shallow etched pits of Si formed by Cu deposition for 20 min; highly localized imprints of Si by Pd NPs with flat Si areas between them; moderately localized Si etching with $Cu_{50}Pd_{50}$ deposition (50/50, 20 min). Scale bar: 100 nm.

The bimetallic deposits also appear in the form of NPs, with diameters and surface coverage that are intermediate between those obtained for Pd and Cu alone. In particular, the average NP size increases (up to ~60-70 nm) with the Pd^{2+} fraction up to (50/50), *i.e.* up to equimolar solution of Cu^{2+} and Pd^{2+}, and then decreases slightly at (75/25) and (100/0). The surface coverage decreases monotonically (from ~30 to 6%) with the increase in the Pd^{2+} fraction. These intermediate characteristics are somewhat predictable. However, the NP morphology is notably different from that of pure metals: the bimetallic NPs show a higher degree of sphericity and a granular shape formed by agglomeration of nanosized elements (clearly seen in Figure 2 for the 50/50 Cu^{2+}-Pd^{2+} mixture). This NP morphology is predominant for bimetallics with a fraction of $Pd^{2+} \geq 50\%$. For Cu^{2+}/Pd^{2+} (75/25), the Cu characteristics predominate.

Another characteristic of the bimetallic deposits (with medium or high Pd content) is a moderate localized etching of Si during metal deposition (see images for bimetallics with Pd^{2+} fraction $\geq 50\%$). The Si etching increases with the deposition time (compare images for a given composition at 5 and 20 min in Figure 1) and is more localized for higher Pd^{2+} fractions. For example, if we compare the deposits obtained in Cu^{2+}/Pd^{2+} (50/50) and in (25/75) after 5 min, the whole Si surface is etched for the (50/50), while only the surface close to the NPs is etched for the (25/75). Similarly, after 20 min, although both samples show significant etching,

the ratio of flat to etched surfaces is higher for (25/75). As for the pure metals, Pd exhibits a very localized etching while Cu shows a shallow delocalized etching. This feature can be observed more clearly in the cross-section images shown in Figure 2.

Influence of the Pd counterion (NO_3^-, Cl^-). Silicon etching is driven by oxidizing agents, the metal cation itself but also H_2O_2, NO_3^-, etc. To investigate whether the particular etching morphology is influenced by the counterion NO_3^- of the Pd salt, Figure 3 compares samples in which CuPd was deposited by using $PdCl_2$ and $Pd(NO_3)_2$ as precursors. The solutions (20 mL) are a mixture of Pd^{2+} and Cu^{2+}, both at 0.5 mmol L^{-1}. The temperature was fixed at 21.0°C (± 1°C) for a rigorous comparison [23]. A similar figure comparing Pd NPs deposited alone in the presence of NO_3^- and Cl^- is given in the SI (Figure S1).

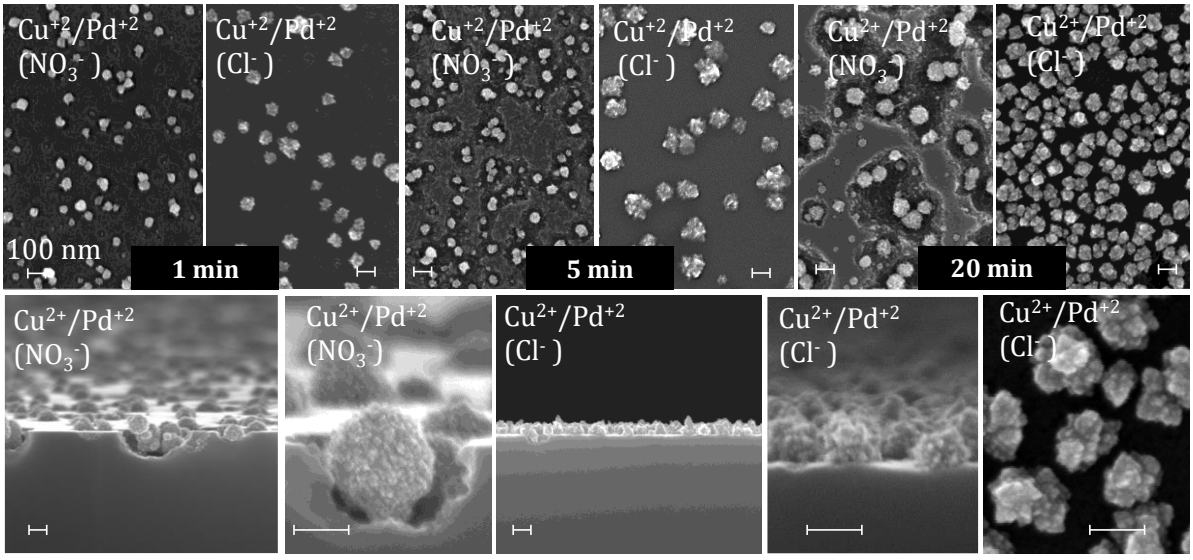

Figure 3. SEM images of Si samples metallized with $CuSO_4$ and $Pd(NO_3)_2$ or $PdCl_2$. Top: Plan-views. Deposition time given on the Figure. Bottom: All the images correspond to 20 minutes deposition. Cross-section and plan-views at different magnifications showing the etching pits and the granular form of the bimetallic NPs. Scale bar: 100 nm. Initial concentration of metal precursors: 0.5 mmol L^{-1} in all cases. Volume of precursor solution: 20 mL. Temperature: 21.0 ± 1°C (thermostatic bath).

Figure 3 shows that in the absence of nitrate, the etching below and around the CuPd NPs is less intense and more delocalized. It is therefore probable that the observed craters are related to an additional etching from the oxidizing nitrates, even at the very low concentration used (0.5 mmol·L^{-1} in this case). Interestingly, the nature of the counterion also affects the morphology of the deposited NPs, resulting in NPs that are fairly spherical in the case of NO_3^- and more dendritic in the case of Cl^-. However, the granular aspect is also observed with Cl^-, indicating that in both cases the NPs are composed of smaller nano-crystallites. These results will be used to explain the de/localized character of Si etching in section 3.4.

Composition of the NPS. The composition of the NPs was analyzed by SEM-EDX. Measurements were made on areas of ~245 x 245 nm^2 or at the level of isolated NPs (*e.g.* spot mark in the inset of Figure 2 for Cu^{2+}/Pd^{2+} (50/50) - 1 min). The results are the same in both cases. Table 1 compares the molar fractions of metal salts in the precursor solutions, the target compositions and the measured EDX values.

Table 1. Molar concentration ratio of metal salt precursors, target composition, and atomic composition of the $Cu_{100-x}Pd_x$ deposits with $CuSO_4$ and $Pd(NO_3)_2$ as precursors, at three deposition times. The samples metallized with $CuSO_4$ and $PdCl_2$ at the molar proportion 50/50 are also included for comparison. EDX determinations were performed by spot analysis on 5 different NPs taken randomly.

Cu^{2+}/Pd^{2+} molar fraction in solution	**Target composition**	**EDX composition *vs.* deposition time**		
		1 min	**5 min**	**20 min**
25 / 75	$Cu_{25}Pd_{75}$	$Cu_{30}Pd_{70}$	$Cu_{25}Pd_{75}$	$Cu_{24}Pd_{76}$
50 / 50	$Cu_{50}Pd_{50}$	$Cu_{55}Pd_{45}$	$Cu_{58}Pd_{42}$	$Cu_{59}Pd_{41}$
75 / 25	$Cu_{75}Pd_{25}$	$Cu_{74}Pd_{26}$	$Cu_{75}Pd_{25}$	$Cu_{60}Pd_{40}$
50 / 50($PdCl_2$)	*$Cu_{50}Pd_{50}$*	*$Cu_{70}Cu_{30}$*	*$Cu_{43}Pd_{57}$*	*$Cu_{46}Pd_{54}$*

The atomic composition measured by EDX agrees very well with the target compositions , *i.e.* the initial molar concentration ratio of the metal precursors, when $CuSO_4$ and $Pd(NO_3)_2$ are used. The only significant discrepancy is observed in the case of $Cu_{75}Pd_{25}$ – 20 min ($Cu_{60}Pd_{40}$). For the deposits obtained with $PdCl_2$ as Pd precursor (images of Figure 3), the compositions are close to the initial Pd^{2+}/Cu^{2+} molar ratio at moderate and long deposition times, but not for 1-min, for which the averaged composition is $Pd_{70}Cu_{30}$. This might suggest an enhancement of the kinetic control for Cu deposition in absence of NO_3^- (i.e. lower deposition rate). Overall, obtaining a given bimetallic composition by means of the MACE method is straightforward.

Hereafter, the figures in section 3.1 correspond to results obtained with $Pd(NO_3)_2$ as Pd precursor for the sake of simplicity. The corresponding results with $PdCl_2$ as Pd precursor are presented in the SI (SEM, XRD).

Crystalline structure. Figure 4a shows the XRD patterns of the metallized Si samples. They all show the characteristic diffraction peaks of a cubic face-centered structure (space group Fm-3m, as for pure Pd and Cu [17,18]). A progressive shift of the diffraction peaks (111, 002, 022, 113, 222) is observed with increasing Pd content. A plot of the lattice parameter obtained as a function of the Pd content (at% of Pd) shows a linear variation (Figure 4b), following Vegard's law [19]. Therefore, the bimetallic NPs obtained by this method are solid solution type alloys. They will now be referred to as $Cu_{100-x}Pd_x$.

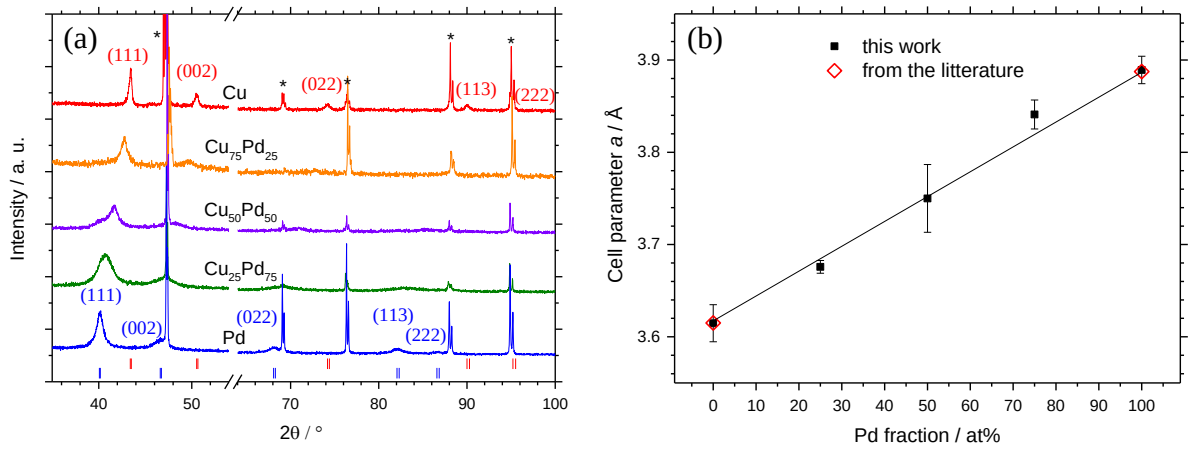

Figure 4. (a) XRD patterns of metallized Si powders obtained by simultaneous deposition. Deposition time: 25 min. $CuSO_4$ and $Pd(NO_3)_2$ concentrations were: 7.5 and 2.5 mmol L^{-1} for Cu^{2+}/Pd^{2+} (75/25), 10 and 10 mmol $L^{-1}$for (50/50), 2.5 and 7.5 mmol L^{-1} for (25/75). HF concentration: 1.5 mol·L^{-1}. Si diffraction peaks are asterisked. Bragg positions of pure Cu and Pd are indicated by double vertical lines (red and blue, respectively). (b) Vegard plot of cell parameter *a* as a function of Pd fraction.

$Pd_{50}Cu_{50}$ synthesized from $PdCl_2$ shows diffraction peaks corresponding to a solid solution type alloy together with a pure Pd phase (Figure S4 in the SI). The fact that the bimetallic NPs obtained in the presence of NO_3^- are pure solid solutions may be related to the additional heat generation during MACE in the presence of this oxidizing counterion[23], which would favor solid solution formation.

3.1.2 Sequential deposition

Figure 5 shows plan-view and cross-section SEM images of metal NPs obtained by sequential deposition, with Cu deposition first, and Pd deposition second in all cases. Three combinations of deposition times were used: Cu^{2+} - Pd^{2+} (1 min - 1 min), (1 min - 5 min) and (5 min - 5 min). The global bimetallic compositions measured by EDX are indicated on the images.

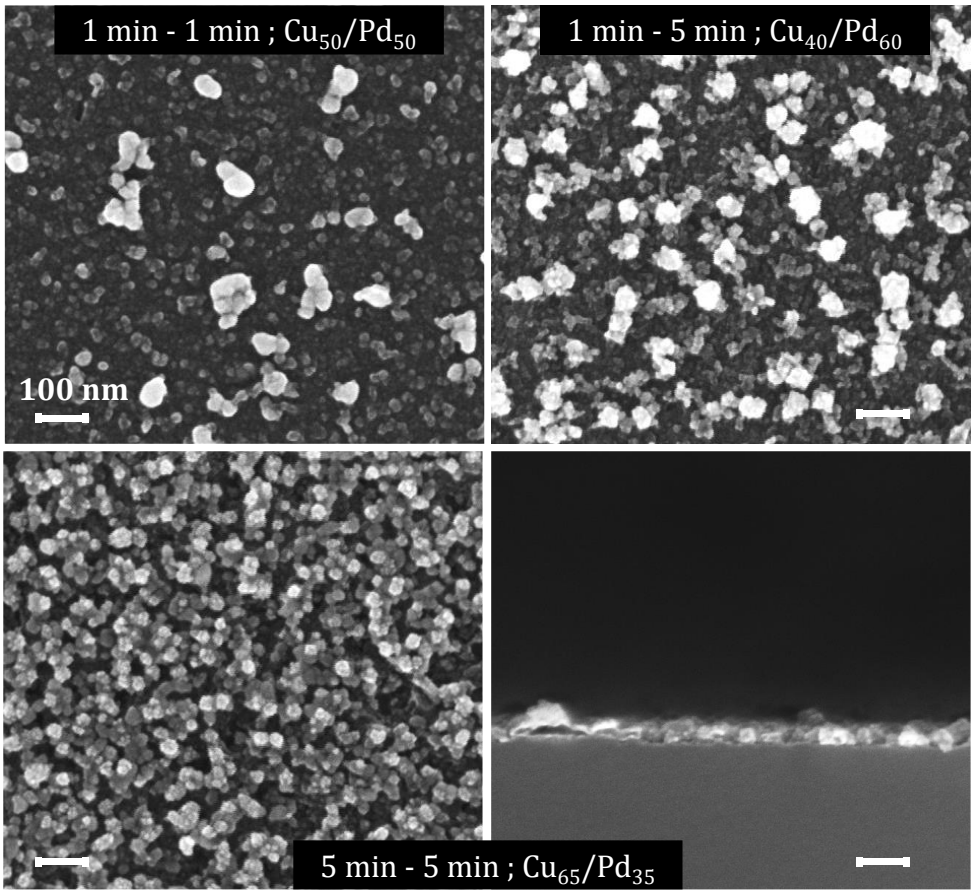

Figure 5. SEM images of the $Cu_{100-x}Pd_x$ bimetallic NPs synthesized by sequential deposition with 1 mmol L^{-1} Cu^{2+} and 1 mmol L^{-1} Pd^{2+} in 1.5 mol L^{-1} HF solution. Scale bar: 100 nm. Global atomic compositions measured by EDX are indicated in the images. Deposition times: Cu^{2+} - Pd^{2+}: 1 min - 1 min, 1 min - 5 min and 5 min - 5 min.

The global composition (measured on 245 x 245 nm^2) is not directly proportional to the deposition times of the metals (Cu^{2+} - Pd^{2+}): Cu_{50}/Pd_{50} for (1 min – 1 min), but Cu_{65}/Pd_{35} for (5 min - 5 min), and Cu_{40}/Pd_{60} for (1 min - 5 min). In addition, there is a significant difference between the global composition and the local compositions measured in spot mode. Sequential deposition results in two different types of NPs: Pd-rich NPs (large and bright in the SEM images), with a Feret diameter of 50-100 nm and a Pd content > 85%, surrounded by Cu-rich NPs (small and dark in the SEM images), with a Feret diameter of 20-30 nm and a Cu content varying from 60-100%. The density of Pd-rich NPs increases from Cu^{2+} - Pd^{2+} (1 min - 1 min) to (1 min - 5 min) as can be expected. Interestingly, the deposit seems to homogenize for (5 min - 5 min), where Pd-rich or Cu-rich NPs can no longer be identified.

Figure 6 shows the XRD diffractograms of metallized Si samples obtained by sequential deposition. In contrast to simultaneous deposition, these samples show the peaks of both pure Pd and Cu phases, indicating phase-separated bimetallic deposits. We have labelled the sequentially deposits as Cu_{100-x}/Pd_x to indicate their non-uniform metal distribution with respect to the solid solution type alloys $Cu_{100-x}Pd_x$ obtained by simultaneous deposition

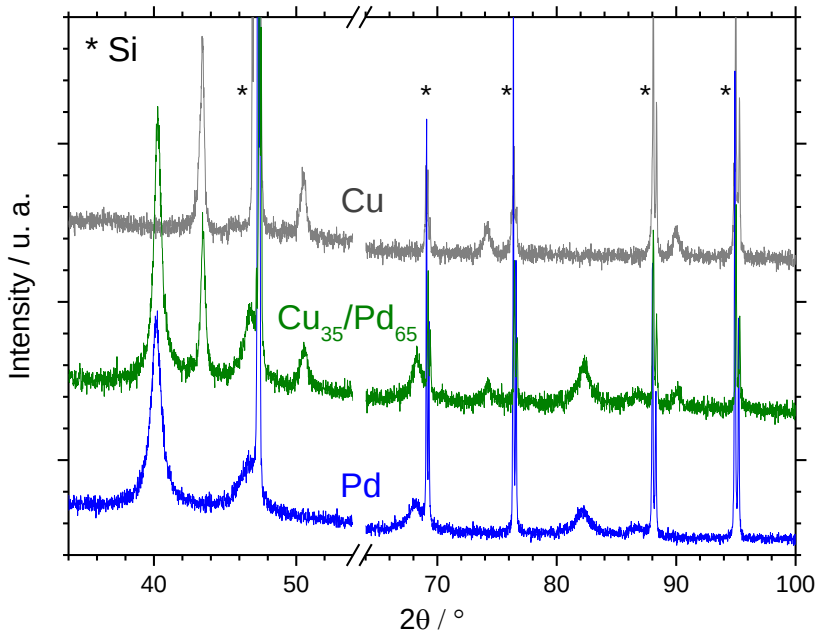

Figure 6. XRD patterns of metallized Si powders obtained by sequential deposition. Deposition time: 5 min / 5 min (Cu^{2+}/Pd^{2+}). Concentrations: 10 mmol L^{-1} Cu^{2+} and 10 mmol L^{-1} Pd^{2+} in 1.5 mol L^{-1} HF solution. Si diffraction peaks are asterisked.

Another difference between sequential and simultaneous deposition is the degree of surface coverage. Almost the entire Si surface is covered by Cu-rich NPs (50 at% Cu) in the sequential mode (see Cu_{50}/Pd_{50} 1 min - 1 min in Figure 5), while well-isolated NPs are obtained in the simultaneous mode (see $Cu_{50}Pd_{50}$ 1 min, in Figure 2). This high density of Cu-rich NPs should be responsible for the shallow etching of Si observed in the cross-section view of the "Cu^{2+} - Pd^{2+} (5 min - 5 min)" sample (Figure 5), very similar to that observed for pure Cu (Figure 2). Finally, the spherical granular shape observed for simultaneous deposition is not found in this case. Similar results are obtained for Si samples metallized with $PdCl_2$ as Pd metal precursor (Figure S3 and S4 of the SI).

In summary, sequential deposition of Cu and Pd can be used to obtain nanoparticulate coatings of phase-separated Cu/Pd alloys instead of a decoration with isolated NPs of Cu-Pd solid solutions.

3.2 Surface composition and oxidation state

The surface composition and oxidation state of the $Cu_{100-x}Pd_x$ and Cu_{100-x}/Pd_x deposits were investigated by XPS. We focus on the range of compositions synthesized by using $Pd(NO_3)_2$ as the Pd precursor (i.e. solid solutions *vs.* separated phases). Figure 7 shows the core spectra of the Cu 2p, Pd 3d, Si 2p and valence band regions (Figure 7a-d, respectively) for samples metallized by simultaneous deposition (*i.e.* $Cu_{100-x}Pd_x$ solid solution type alloys). Figure S5 in the SI shows the core spectra of the Cu 2p and Pd 3d regions of samples metallized by sequential deposition (*i.e.* Cu_{100-x}/Pd_x phase-separated NPs).

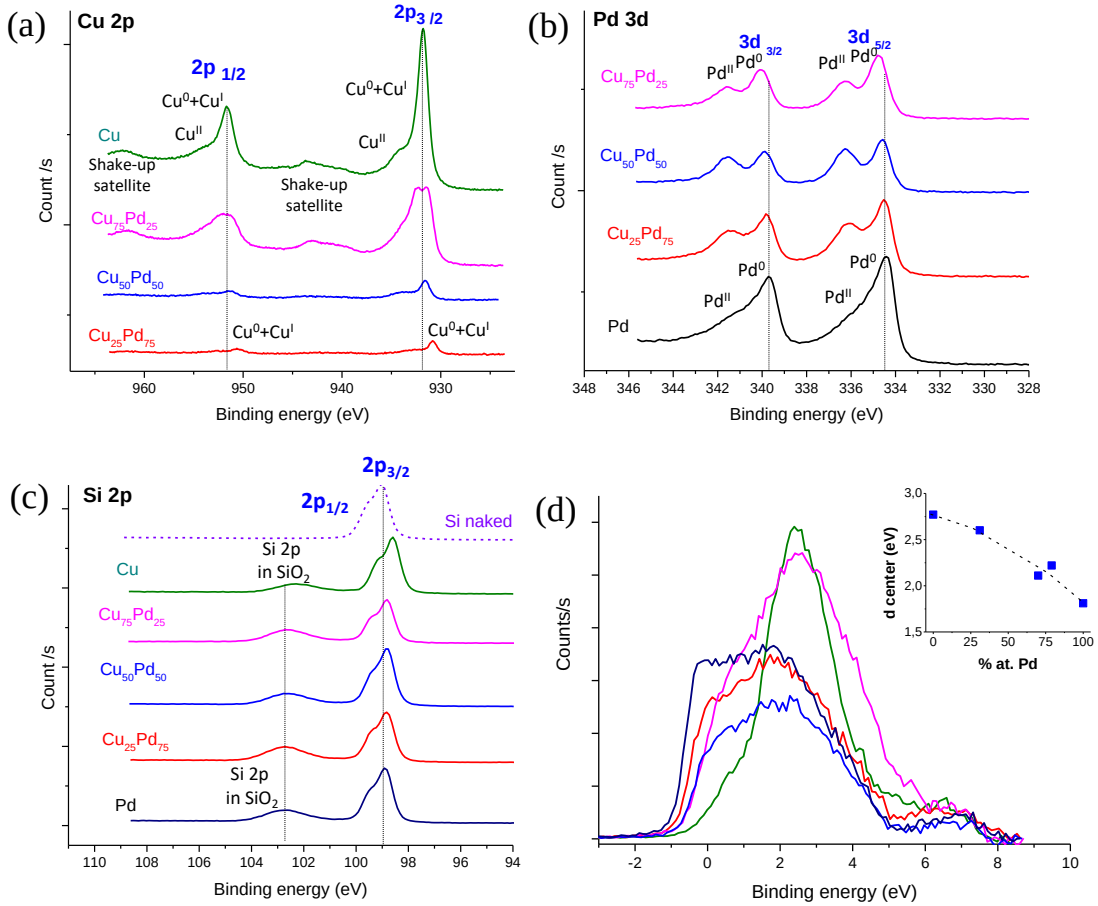

Figure 7. XPS spectra of $Cu_{100-x}Pd_x/Si$ samples obtained by 1 min simultaneous deposition. (a) Cu 2p, (b) Pd 3d, (c) Si 2p and (d) valence band region. Inset of (d): d-band center energy vs. Pd fraction calculated by XPS (see Table 2).

Surface compositions. Table 2 gives the atomic composition of the $Cu_{100-x}Pd_x$ bimetallics quantified by XPS and by EDX-SEM for simultaneous and sequential deposition of Cu and Pd.

Table 2. Bimetallic composition targeted, determined by EDX-SEM and by XPS. Simultaneous deposition for 1 min. Sequential deposition for different durations.

Simultaneous deposition			**Sequential deposition**		
Targeted	XPS	EDX	**Sequence Cu – Pd**	**XPS**	**EDX**
$Cu_{75}Pd_{25}$	$Cu_{68}Pd_{32}$	$Cu_{74}Pd_{26}$	1 min – 1 min	Cu_{67}/Pd_{33}	Cu_{50}/Pd_{50}
$Cu_{50}Pd_{50}$	$Cu_{33}Pd_{67}$	$Cu_{55}Pd_{45}$	1 min – 5 min	Cu_{46}/Pd_{64}	Cu_{40}/Pd_{60}
$Cu_{25}Pd_{75}$	$Cu_{21}Pd_{79}$	$Cu_{30}Pd_{70}$	5 min – 5 min	Cu_{60}/Pd_{40}	Cu_{65}/Pd_{35}

In the case of simultaneous deposition, the surface composition (XPS) is systematically richer in Pd compared to the bulk composition of the alloy (SEM-EDX), probably due to some Cu losses at the surface, since Cu is more easily oxidized than Pd. Ar-plasma etching was performed to etch a couple of nm from this sample and the bulk composition was partially recovered ($Cu_{44}Pd_{56}$, see Figure S8 in the SI), confirming that the excess of Pd is only at the surface. It is not possible to compare the bulk and surface compositions of sequential deposits because they are not homogeneous. For example, in the case of Cu^{2+} – Pd^{2+} (1 min – 1 min), the global composition is Cu_{50}/Pd_{50}, but the surface appears to be richer in Cu, because Cu deposited all over the surface, while Pd formed NPs only in some places (see Figure 5).

Shifts in binding energy. The XPS spectra of Cu 2p (spin orbit doublet $2p_{3/2}$ -$2p_{1/2}$) in Figure 7a show three contributions related to (Cu^0 + Cu^I) at 931.9 and 951.7 eV, Cu^{II} at 934.1 and 954 eV [24–26], and satellites corresponding to shake-up transitions (in the case of pure Cu and $Cu_{75}Pd_{25}$). As the bimetallic becomes Pd-rich, the intensity of the Cu 2p lines decreases and their position shifts to lower binding energies (-0.8 eV for $Cu_{25}Pd_{75}$ *vs.* pure Cu). The core level of Pd 3d (Figure 7b) exhibits two well-defined doublets $3d^{5/2}$ - $3d^{3/2}$ corresponding to Pd^0 and Pd^{II} in the bimetallics, and an asymmetric peak that includes the two valent state contributions for pure Pd (334.4 and 339.6 eV) [24–26]. A positive shift in the binding energy is observed as the Cu content increases (*e.g.* +0.2 eV from pure Pd to $Cu_{75}Pd_{25}$), with a decrease in the peak height. These opposite shifts in the Cu 2p and Pd 3d core lines are attributed to the withdrawal of valence electrons from Pd 4d to half-empty Cu 4s upon bonding of the two metals, as reported for CuPd bimetallics in different configurations, *e.g.* supported bimetallic CuPd thin films [27], Cu-modified Pd NPs (unalloyed) [18], or CuPd nanoalloys [28].

The spectra of the samples metallized by sequential deposition (Figure S5 of the SI) are similar to those obtained by simultaneous deposition, *i.e.* it shows the two contributions (Cu^0 + Cu^1) and Cu^{2+} in the Cu 2s core spectra. The contribution of the peaks corresponding to the

PdO and CuO oxides is higher in the bimetallics than in the pure metals. Interestingly, the peaks in the core spectra of Pd and Cu atoms appear shifted with respect to pure metals, as observed for the solid solution type alloys, but with a slightly smaller magnitude: maximum shift of +0.6 eV for Cu $3p^{3/2}$ *vs.* pure Cu and -0.1 eV for Pd $3d^{5/2}$ *vs.* pure Pd in "Cu^{2+} –Pd^{2+} (1 min – 5 min)", *i.e.* Cu_{46}/Pd_{64}. These shifts indicate a net charge transfer from Pd to Cu atoms in close proximity, even if they do not share the same lattice [18,27].

Figure 7c shows the core level spectrum around the Si 2p. It evidences an oxide-free surface for bare Si with a Si $2p^{3/2}$ – $2p^{1/2}$ centered at 99.3 eV [24]. After metal deposition, a shift of this peak to slightly lower binding energies is observed, as a result of the metal contact (as in the case of Au deposition on Si [12]). A new peak corresponding to SiO_2 also appears in all cases. This is probably related to the roughening of the Si surface (Si dissolution during metal deposition), which leads to a larger amount of oxidized Si under air exposure compared to polished bare Si [12].

Valence band spectra and d-band center. Figure 7d shows the valence band spectra (VBS) of the $Cu_{100-x}Pd_x$ /Si samples. The inset shows the evolution of the d-band center position with the fraction of Pd. The d-band center has been calculated from the XPS spectra as the weighted average energy of the VBS after a Shirley-type background has been subtracted [28–31]. The details of the calculation are given in the SI. Consistent with the shift observed in the Pd 3d and Cu 2p core lines, a gradual shift in the position of the d-band center from pure Cu (2.77 eV) to pure Pd (1.81 eV) is observed, in agreement with values reported by other authors [28,29]. It should be noted that several factors such as the NP size, residual gas adsorbates or the limits selected for VBS integration can affect this parameter [18,29,32].

The effective d-band center values obtained for the bimetallic sequential deposits are plotted against the surface atomic compositions measured by XPS in Figure S6 of the SI. These atomic compositions are global, since the sequential deposits do not have a homogeneous composition the entire sample (as described in the SEM-EDX section). For the same reason, the obtained d-band center values must be considered as averages over the area scanned by XPS (a few hundred of μm^2), *i.e.* as apparent d-band center positions. Nevertheless, they can be useful to describe the global properties of the bimetallic surface. The values obtained are well between those of pure metals and are in line with those obtained for similar atomic compositions in simultaneous deposition (indicated by crosses).

According to the d-band center theory, the lower the center level with respect to the Fermi level (*i.e.* 0 of the valence band energy) of a given metal, the stronger the bond formed by the metal to a given adsorbate (related to the occupancy of antibonding states [30]), which ultimately leads to surface poisoning. It is well known that Pd is easily poisoned during CO_2RR by CO adsorption [33,34], and that the addition of a moderate fraction (~15–25% at%) of Cu atoms (low CO adsorption energy compared to Pd), can partially protect Pd from CO-poisoning while maintaining its low overpotential for CO and HCOOH formation [34–36]. We have recently demonstrated by CV measurements that the resistance of CuPd NPs to CO poisoning follow a volcano plot upon addition of Cu, tipping at the composition $Pd_{30}Cu_{70}$ [19], in agreement with other studies [28]. According to the values obtained by XPS, this composition corresponds to an alloy d-center position of ~2.1 eV, which would provide a near-optimal CO binding energy (Wang et al. found 2.18 eV for an optimal composition of $Cu_{20}Pd_{80}$ [28]).

3.3 Electrochemical features of metal deposition on Si

The SEM images given in Figure 1 show that Cu alone is deposited on the entire Si surface, whereas in the presence of Pd (≥ 50% at.), Cu is only found at the level of the CuPd NPs. This raises the question: how is Cu deposition prevented between CuPd NPs?

When p-type silicon is put in contact with a noble metal in HF solution containing an oxidizing agent a galvanic cell is formed, i.e. there are anodic and cathodic sites on the semiconductor surface with local cell currents flowing between them [37,38]. The oxidizing agent in our case is the noble metal ion in solution. The electroless Si dissolution occurs at open-circuit-potential (OCP), that is, the rate of hole consumption (Si oxidation) is equal to the rate of hole injection in the Si valence band (metal ion reduction). Thus, monitoring the OCP during metal deposition is useful to gain insight in the mechanism of the reaction, such as the rate-controlling reaction steps (thermodynamics, kinetics or mass transport) and their evolution with time [39]. The OCP is the mixed redox potential resulting from the equilibration of negative charge transfer (metal ion reduction, Eq. 1) at cathodic surface sites and positive charge transfer (Si dissolution, Eq. 2) at anodic surface sites of the Si electrode [2,40]:

$$\mathrm{E}_{OCP} = \frac{1}{2}\left(\mathrm{E}^{eq}_{SiF_6^{2-}/Si} + E^{eq}_{M^{2+}/M}\right) + \left(\frac{\mathrm{RT}}{nF}\right)\ln\left(\frac{j_{0C}}{j_{0A}}\right) \qquad \text{Eq. 4}$$

where $E^{eq}_{SiF_6^{2-}/Si}$ and $E^{eq}_{M^{2+}/M}$ are the equilibrium redox potentials in the specific conditions of metallization (thermodynamic terms), j_{0C} and j_{0A} the corresponding exchange current densities (kinetic terms). $E^{eq}_{M^{2+}/M}$ is given by:

$$E^{eq}_{M^{2+}/M} = E^{0\prime}_{M^{2+}/M} + \left(\frac{0.059}{2}\right) log([M^{2+}]) \quad \text{Eq. 5}$$

where $E^{0\prime}_{M^{2+}/M}$ is the formal redox potential of Cu^{2+}/Cu and Pd^{2+}/Pd (+0.14 V and +0.75 V *vs.* Ag/AgCl, respectively) and $[M^{2+}]$ its concentration in solution. We determined $E^{eq}_{Cu^{2+}/Cu}$ and $E^{eq}_{Pd^{2+}/Pd}$ experimentally as +0.02 V and +0.62 V *vs.* Ag/AgCl, respectively, by using a Cu or a Pd wire in contact with the corresponding deposition solution (*i.e.* 1.5 mol L^{-1} in HF and 1 mmol L^{-1} in $CuSO_4$ or $Pd(NO_3)_2$).

Figure 8 a-c and e-f shows the OCP evolution during Cu, Pd, and $Cu_{50}Pd_{50}$ deposition with the different metallic salts used. Figure 8d shows the electrochemical Si dissolution curve in 1.5 mol L^{-1} HF together with the experimentally determined $E^{eq}_{Cu^{2+}/Cu}$ and $E^{eq}_{Pd^{2+}/Pd}$ values (*i.e.* before contact between the metal and Si, given by an orange and a red bar, respectively). This last figure helps visualizing the semi-reactions involved in the galvanic cell formed (i.e. Si dissolution and metal cation reduction) and interpreting the OCP attained when the reactions are coupled.

The Si samples were initially immersed in the HF solution. At the beginning, the OCP is determined by the anodic dissolution of Si and the hydrogen evolution reaction (~ -0.25 V *vs.* Ag/AgCl) [39]. The dissolved metal salt is injected at t = 0 s. The OCP increases upon injection due to the enhanced cathodic current as metal ions are reduced at the Si surface, balanced by a higher Si dissolution current (see the inset of Figure 8d), establishing the mixed redox potential as described in Eq. 4. In addition, there is also H_2 evolution on the metal NPs in parallel to metal cation reduction. What are the respective shares of these two components in the cathodic current is a complex question [1,41]. In the following, we assume that the variations of OCP after the initial shift are mainly related to the reduction of metal cations. For the solutions containing a Pd salt, the discussion is then rigorously applicable to the case in which $PdCl_2$ is used as metal precursor (Figure 8a and b), given the observed influence of NO_3^- counterion in the deposition rate and morphological characteristics. Nevertheless, the OCP curves do not change significantly by the presence of NO_3^- or Cl^-, especially in the case of CuPd deposition (Figure 8b and f), which might indicate that NO_3^- affects mainly the metal deposition at the level of the Si surface.

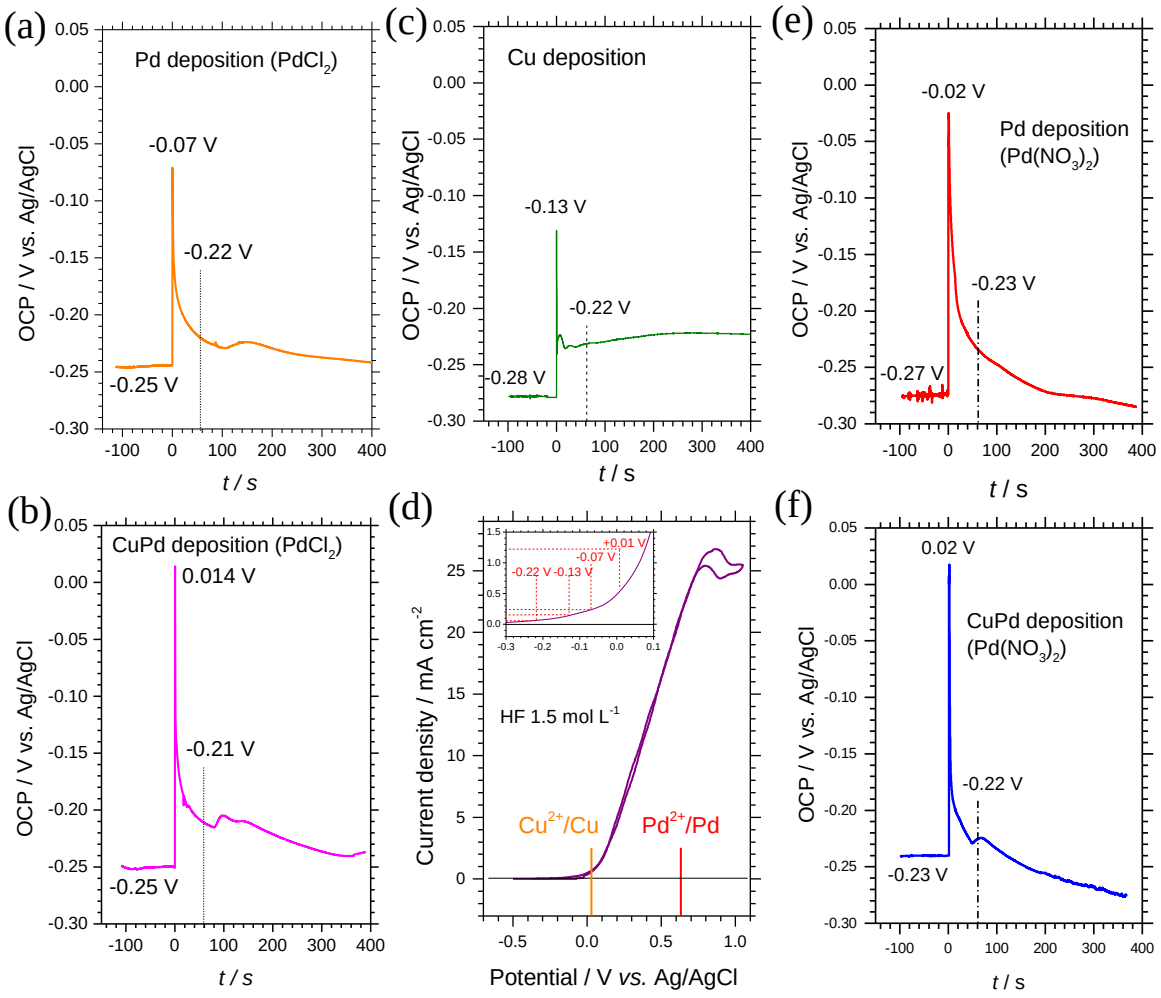

Figure 8. Evolution of OCP during metallization of Si substrates in 1.5 mol L^{-1} HF solutions with (a) Pd^{2+} (from $PdCl_2$), (b) equimolar mixture of Cu^{2+} and Pd^{2+} (from $PdCl_2$), (c) Cu^{2+}, (e) Pd^{2+} (from $Pd(NO_3)_2$) and (f) equimolar mixture of Cu^{2+} and Pd^{2+} (from $Pd(NO_3)_2$). All the solutions are at concentration 1 mmol L^{-1} for the metal precursors. (d) Voltammogram of the p-type Si substrate in 1.5 mol L^{-1} HF showing the redox potentials determined for Cu^{2+}/Cu and Pd^{2+}/Pd, with Cu and Pd wires. Inset: Focus on the onset potential region.

In the case of Pd (Figure 8a), after its initial positive increase, the OCP gradually shifts to negative values. This is due to the depletion of Pd^{2+} ions, which lowers $E^{eq}_{Pd^{2+}/Pd}$, according to Eq. 5, as well as the cathodic exchange current density j_{0C}. Pd follows a progressive mode of nucleation and growth with well separated NPs [4]. In the case of Cu (Figure 8b), the OCP remains constant after the first spike. It has been reported that Cu exhibits an instantaneous nucleation mode with deposition over the entire Si surface [4]. This should hinder the access of the (HF) electrolyte to the Si surface, limiting severely the anodic exchange current (j_{0A}) and thus the Cu deposition rate. The Cu^{2+} surface concentration is then relatively stable and the OCP remains approximately constant at a slightly less negative value than before the Cu salt

injection (-0.22 V *vs.* Ag/AgCl). The SEM images after Cu deposition (Figure 1) show the fusion of Cu NPs into continuous agglomerates (or even films). This could be related to the high surface diffusivity of Cu atoms at Cu surfaces in acidic media (1.79 10^{-16} m^2 s^{-1}) [42]. The OCP of CuPd (Figure 8c) shows a similar behavior to that of Pd, with an initial positive increase up to +0.02 V followed by a gradual decrease.

The inset of Figure 7d shows a focus in the onset potential region, where the initial OCP values at the injection spike (t=0) for CuPd and Pd (obtained from $PdCl_2$) and Cu are indicated. The values are +0.01, -0.07 and -0.13, respectively, corresponding to a higher initial Si dissolution current for CuPd than Pd and Cu. After 1 min of deposition, all the OCPs reach a similar value (~ -0.22 V, also indicated on the inset), which corresponds to a polarization of the Si bulk of ~0.05 V with respect to the initial OCP before injection.

Interestingly, the dendritic shape of pure Pd NPs disappears with the addition of Cu. The absence of Cu except in CuPd NPs indicates that Pd acts as a Cu sink. We suggest that the fundamental reason for the absence of Cu deposition between CuPd NPs is the more noble character of Pd (E^0 Cu^{2+}/Cu = +0.14 V and E^0 Pd^{2+}/Pd = +0.75 V *vs.* Ag/AgCl, respectively). On this basis, several mechanisms can intervene: (1) oxidation of Cu nuclei by galvanic displacement with Pd^{2+} and NO_3^-, (2) increase of the ohmicity of the CuPd/Si junctions (causing anodic polarization of their surroundings) which does not favor Cu^{2+}reduction/deposition between CuPd centers, (3) Cu^{2+} mass transport (either redissolved or coming from the solution bulk) towards CuPd centers, where CuPd NPs are protected from oxidation/dissolution by the noble nature of Pd. Since Cu^{2+} and Pd^{2+} have similar diffusion coefficients (7.1 and 8.3 10^{-6} cm^2 s^{-1}, respectively [43,44]), the result of this interplay is a NP composition that depends directly on the molar ratio of Cu^{2+} and Pd^{2+} in the precursors solution, as shown in Table 1.

3.4 Localization of MACE (Band bending modelling)

MACE of Si is extremely localized with Pd NPs deposited from $Pd(NO_3)_2$ (*cf.* Figure 1 and Figure 2) and rather delocalized with Pd NPs deposited from $PdCl_2$ (Figure S1). High work function metals are usually characterized by delocalized MACE of p-type Si due to the ohmic character of the p-Si/metal junction. For example, Pt NPs "chemically polarized" with H_2O_2 (in HF-H_2O_2 solutions) act as anodically polarized "ohmic back contacts", resulting in the anodic polarization of the entire Si sample and thus in delocalized etching [21]. Conversely, highly localized etching is observed for metals with lower work functions such as Ag (4.6 eV *vs.* 5.6 eV for Pt) [20]. Since Pd has a large work function (5.12-5.22 eV [45–48]), delocalized etching is expected, on the contrary to what was reported by Yae et al. [49]. A comparison between Pt

and Pd NPs deposited under the same conditions is shown in Figure S7 of the SI. It is clear that the Si surface between the NPs is etched (rough) in the case of Pt and Pd obtained from $PdCl_2$, whereas it remains mostly flat (with some pits) in the case of Pd obtained from $Pd(NO_3)_2$. Cross-section images show dissolution craters under each Pd NP obtained from $Pd(NO_3)_2$ (localized etching), but not under Pt NPs, and not under Pd NPs obtained with $PdCl_2$ (except for a few craters). The reason of this particular behavior of Pd is unknow. We hypothesize that it could be the formation of Pd hydride, PdHx, due to the presence of hydrogen evolution during Si etching. The work function of PdHx is 0.2 eV lower than that of Pd [45]. This property has been used to design electronic hydrogen sensors based on the conductivity of a Si thin film (50 nm) containing Pd NPs, which produce a chemical gating effect when forming PdHx in the presence of hydrogen [50]. The formation of PdH_x would be enhanced when NO_3^- is present in the reaction media, due to the higher amount of H_2 produced because of the additional Si etching induced by this counterion.

In an attempt to explain the peculiarities observed for Pd deposition by MACE, we have modeled the Pd/p-Si/Electrolyte interface at the nano- and micro-scales. Numerical simulations were performed using SILVACO© ATLAS, a TCAD simulation software (see the Section 6 of the SI for more details). The modeled Pd/p-Si/Electrolyte (HF) structure consists of a Pd pad on flat Si surrounded by two short-circuited electrolyte contacts with a total width of 1 µm (*cf.* Fig. S6 in the SI). The metal and electrolyte electrodes are separated by a gap of 1 nm to ensure that charge transfer only occurs through the Si/Electrolyte and Si/Pd interfaces. To mimic deposition by MACE, a positive polarization is applied between the metal and the electrolyte. Mott-Schottky plots and KP-AFM measurements were performed to obtain the electrolyte and metal work function values required for the simulations (*cf.* Section 6 of the SI). The localization of MACE depends on Si doping. More precisely, the porous structure of the product is dependent on the space-charge layer, which is controlled by the Si doping and the chemical identity of the deposited metal [23]. For the simulations this value has been kept constant to 1×10^{15} cm^{-3} (doping of the p-Si used for the experiments).

Figure 9 shows the effect of the metal work function, W_m, on the valence band (VB) profiles of the Metal/Si and Si/Electrolyte junctions. The profiles correspond to the band bending along a cutline (y-coordinate) going from the border of the NP (x=0.550 µm) to bulk Si (10 µm in depth) and back to the adjacent border of the electrolyte (x=0.553 µm), *i.e.* at a lateral distance of 3 nm (see Figure 9a inset). Three W_m values were chosen according to the previous discussion: 5.20 eV, a typical value for Pd (Figure 9a); 4.92 eV, the value determined by KP-AFM measurements (Figure 9b); and 4.73 eV, the experimental value minus 0.25 eV,

corresponding to a hypothetical PdH_x (Figure 9c) generated during MACE deposition. The latter value is also consistent with Cu, for which the KP-AFM measurement gave 4.77 eV.

The VB profiles are shown for three polarizations applied to the metal NP *vs.* the Electrolyte, to account for the conditions during metal deposition: 0 V (equilibrium, solid black lines); +0.05 V (dashed green lines), similar to the polarization observed after 1 min of deposition in the OCP curves in Figure 8a-c; +0.20 V, close to the polarization observed in the first moments of metal deposition for Pd in Figure 8a (red solid line).

Metal NP with W_m = 5.20 eV, Figure 9(a). At equilibrium (0 V), the edge of the VB (black dot) at the NP border is at +0.03 eV above the Fermi level (solid black lines). This indicates that Si is degenerated, with a strong accumulation of h^+ under the metal NP, *i.e.* the Metal/Si junction behaves as an ohmic contact, as already reported for Pt under MACE conditions [21]. Therefore, h^+ can easily be injected from the NP into the Si bulk (zero energy barrier). On the contrary, the Si/Electrolyte junction behaves like a Schottky diode, with an energy barrier for h^+ diffusion from the Si bulk to the electrolyte ("at 0V" arrow). Note that two local minima of the VB are observed, near the Metal/Si and the Si/Electrolyte contacts (y ~ 0.1 and 19.9 µm). They are mainly due to the small distance between the NP and Electrolyte boundaries (3 nm) considered in these profiles. The band bending of the junctions affect each other laterally and results in these VB modulations [20]. The effective barrier heights are calculated considering these minima. Indeed, at the Si/Electrolyte interface, it is the effective barrier that must be taken into account, because the remaining potential drop at the interface itself is thin enough for h^+ tunneling to the electrolyte (thermionic field emission transport mechanism) [20]. Table S5 in the SI gathers the effective barrier height values obtained.

When the NP is polarized (*e.g.* by +0.20 V *vs.* the electrolyte, solid red lines), the Si bulk is polarized to the same extent due to the ohmic nature of the Metal/Si contact, *i.e.* the effective barrier heights at the Si/Electrolyte (Schottky) junction is reduced from 0.170 eV (0 V) to 0.06 eV ("at 0.2 V" arrow). The overall result is consistent with a delocalized etching, intense at the border of the NP but also significant far from it, as shown in Figure S12 of the SI by the VB profiles connecting the center of the NP with the center of the electrolyte. The values in Table S4 show that for W_m = 5.20 eV, the effective barrier height in the center of the electrolyte also decreases significantly with polarization.

Metal NP with W_m = 4.92 and 4.73 eV, Figure 9(b, c). At equilibrium (0 V), the VB edges at the NP border (black dots) are below the Fermi level, at -0.25 and -0.44 eV, respectively, and the contact with Si is no longer ohmic. Thus, the Metal/Si and Si/Electrolyte junctions correspond to two Schottky diodes back-to-back. The effective barrier height at the

Metal/Si junction ("at 0 V" arrow) is 0.47 eV for W_m = 4.92 eV (b) and 0.54 eV for W_m = 4.73 eV (c), which plays against the diffusion of h^+ from the NP to the Si bulk (*cf.* Table S5). At the Electrolyte border, the VB edge is always at 0.67 eV (blue dot, irrespective of W_m and the polarization). The effective barrier height for h^+ diffusion to the Electrolyte is ~0.23 eV for W_m of 4.92 eV and ~0.33 eV for W_m = 4.73 eV. The progressive increases in barrier height at each border when W_m decreases suggest a less delocalized etching.

When W_m decreases, the effect of the NP polarization on the effective barrier height of the Si/Electrolyte junction (which controls the h^+ diffusion and etching at the level of the electrolyte) is also much weaker than in the case of an ohmic contact. For instance, at +0.20 V, the effective barrier height is 35% of its initial value (at 0 V) for W_m = 5.20 eV, 54% for W_m = 4.92 and 77% for W_m = 4.73 eV. This is due to the reinforced Schottky character of the metal contact when W_m decreases.

These results suggest a moderately delocalized etching for the metal with a W_m = 4.92 eV, consistent with the observations on Pd deposition in the presence of Cl^-, and a more localized etching for the metal with W_m = 4.73 eV (corresponding to the hypothetical PdH_x) consistent with the observations on Pd deposition in the presence of NO_3^-.

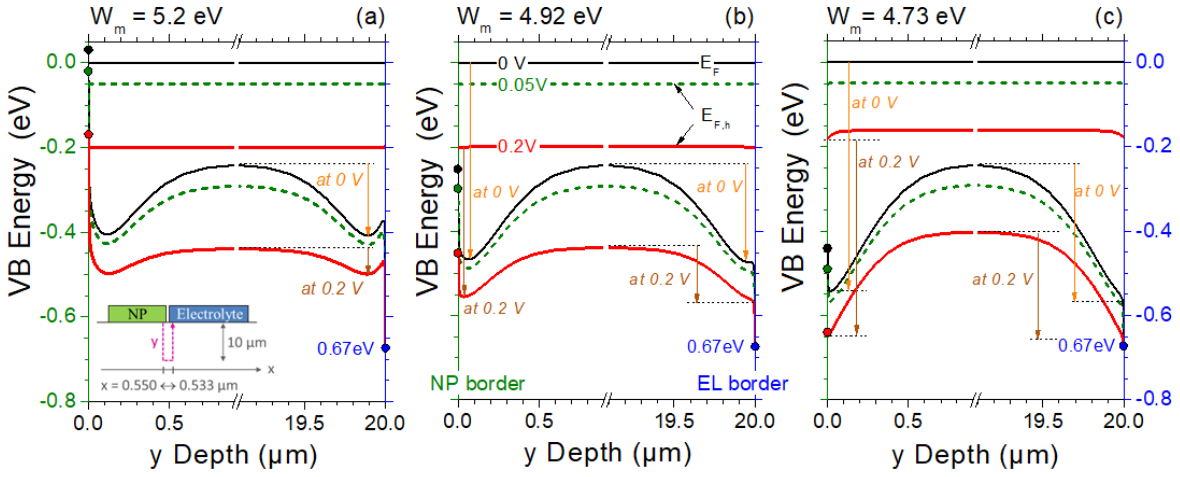

Figure 9. Valence band profiles of the modeled "NP (border)/p-Si/Electrolyte (border)" systems at equilibrium (0 V, black solid lines) and under polarization of the NP *vs.* Electrolyte by +0.05 V (green dashed line) and +0.20 V (red solid lines). *x* is the lateral position on the device surface (width) and *y* is the position along the cutline through bulk Si, as schematized by the inset in (a). See also *Section 6* of the SI. Three work function values were chosen for the metal NP: (a) 5.20 eV (typical value for Pd), (b) 4.92 eV (Pd measured by KP-AFM) and 4.73 eV (hypothetical Pd-H_x).

To extend the information given in Figure 9, the lateral modulation of the VB energy (x-cutline at 1 nm below the Si surface) at the level of a metal NP surrounded by the electrolyte is shown in Figure 10, for the three selected W_m and polarization values. The VB level is

referenced to the VB energy in the Si bulk (where it is set to zero), *i.e.* the value represents the energy barrier height seen for h^+ coming from the Si bulk.

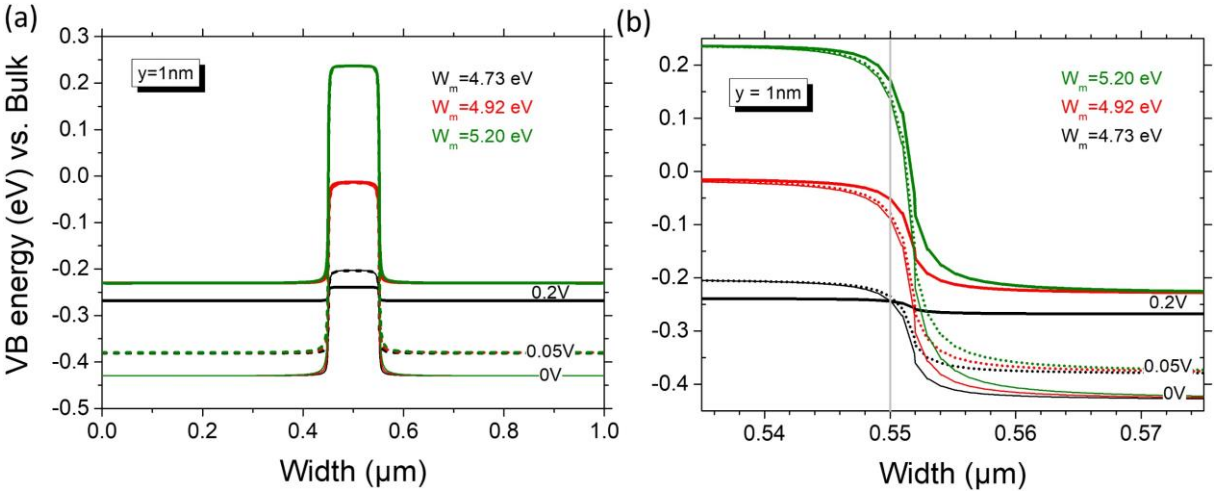

Figure 10. (a) Lateral modulation (x-width) of the VB energy at 1 nm below the Si surface. Other conditions are set as in Figure 9. (b) Zoom on the metal NP region. A vertical grey line at x=0.55 µm indicates the NP border. The valence band energy is here referred to valence band in the Si bulk (different from Figure 9).

At 0 V and 0.05 V, there is no difference between the VB energies at the electrolyte level, whatever the W_m (all curves overlap at 0 V and idem at 0.05 V). Thus, regardless of whether the Si/Metal contact is ohmic or Schottky, the Si etching during deposition is localized at the edges of the NP where the h^+ come from (h^+ have an energy barrier around 0.45 eV to reach the electrolyte interface). When approaching the NP border (x = 0.55 µm), the VB reaches its value at the NP/Si interface depending on W_m : no barrier for W_m = 5.20 eV, and presence of a barrier for h^+ coming from the Si bulk for W_m = 4.92 eV (between 0.1 - 0.2 eV) and 4.73V (between 0.2 - 0.4 eV). Zooming into the NP region (Figure 10b) shows that the potential drop is more abrupt at the NP border (at x = 0.55 µm) for the metal with W_m = 4.73 eV, consistent with a more localized etching. At a stronger polarization, 0.2 V, a difference in the VB energy at the level of the electrolyte is observed for W_m = 4.73 eV, with a VB energy 0.1 eV higher (in absolute value), *i.e.* an energy barrier height higher for h^+ in the Si bulk, with respect to W_m of 5.20 and 4.92 eV. It is therefore logical to assume that for a Si/Schottky junction (4.73 eV), the etching is localized next to the NP, confirming that, in the presence of NO_3^-, Pd should have a low W_m value. On the contrary, the etching is rather delocalized for a Si/Schottky junction with 4.92 eV, which confirms that in the absence of NO_3^- the W_m value of Pd NPs is close to that determined by KPFM measurements. These results support the hypothesis of PdH_x formation, being accentuated in presence of NO_3^-. Nevertheless, further experiments would be required to confirm it.

We also observe that MACE of Si with Cu NPs is not localized. However, it is known that Cu (W_m of ~4.7 eV in the literature [45–48]) forms a Schottky junction with p-type Si, which should result in localized MACE of Si, as it is the case with Ag (~4.6 eV). Closer examination of the Cu NPs/Si interface in the cross-section image of Figure 2 (Cu^{2+} 20 min) shows that the morphology of the Cu deposit may be imprinted in Si, but at a very shallow depth. Indeed, Chemla et al. have reported that in dilute HF solutions with traces of Cu^{2+} (less than 10 µmol L^{-1}), Cu nuclei form on Si and are often surrounded by a corrosion pit [2]. We can assume that in our case no localized etching occurs due to the instantaneous nucleation of Cu, which results in very small Cu NPs covering the entire Si surface and thus smoothing the surface during etching. Due to the density of Cu NPs on the surface, it is also possible that the modulation of the VB has an influence on the etching result.

Figure 11a-c shows this phenomenon from 2D images of the VB energy variation laterally and in depth (taken at 10 nm below the surface), for a structure with one, three and fifteen nanoparticles. Figure 11b and c correspond to two different NP distributions with the same surface coverage (of 30%). In all cases, a polarization of 0.05 V is applied to mimic the deposition conditions, and W_m is chosen to be 4.73 eV (very close to the 4.77 eV determined here by KP-AFM). The energy values are referenced to bulk Si (0 eV, as in Figure 10) and are shown on a color scale: green indicates regions where there is no energy barrier for diffusion of h^+ coming from the bulk, and dark blue indicates regions where the energy barrier is high.

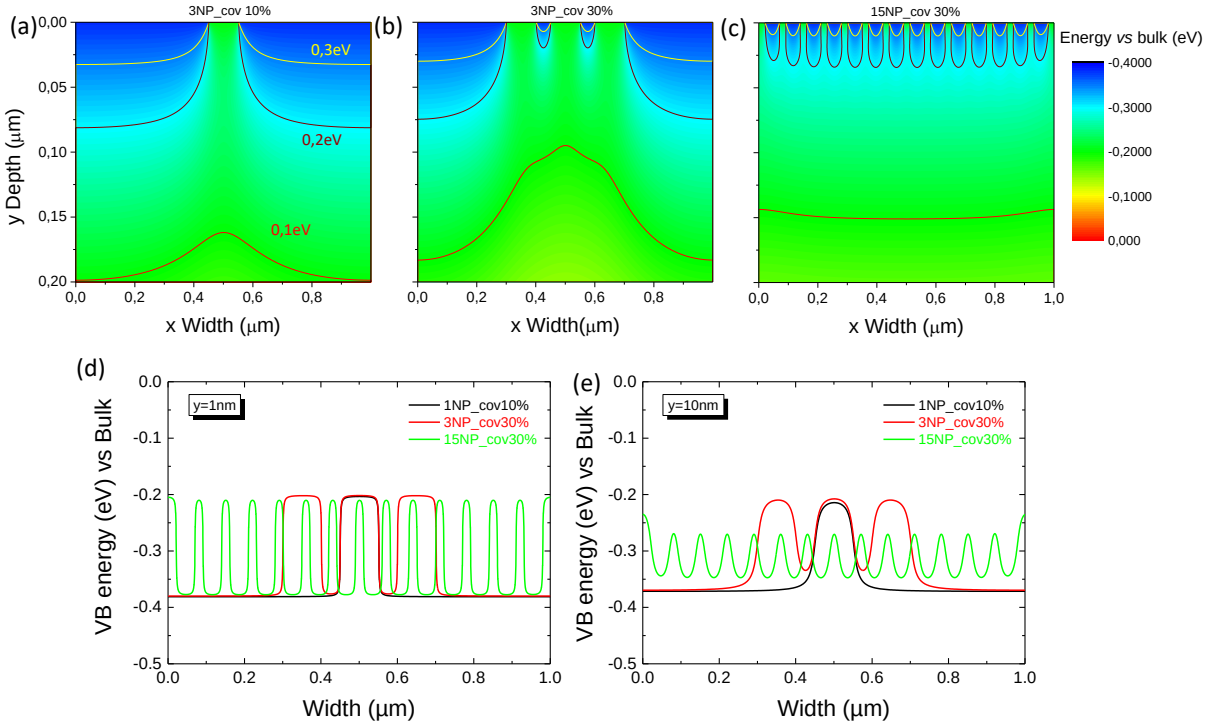

Figure 11. 2D VB profiles (VB energy *vs.* bulk) at 10 nm below the Si surface for a structure with one (a), three (b) and fifteen (c) NPs. (d and e) Lateral modulations (x width) for the structure with fifteen NPs at 1 and 10 nm below the Si surface. The polarization is 0.05 V in all cases and Wm = 4.73eV. Figures (b) and (c) have the same surface coverage: three NPs of 100 nm each and fifteen NPs of 20 nm each (see SI (Figure S9) for more details on the modeled device).

From these images we observe a significant modification of the barrier height variation with the number of NPs (both laterally and in-depth) in the subsurface under the NP (up to 200 nm depth). This effect is clearly visible if we compare the changes of the iso-energy barrier height of 0.3, 0.2 and 0.1 eV (represented by yellow, wine, and red color lines, respectively) between the 2D VB profiles shown in Figure 11a-c. Therefore, these modulation changes in VB energy can have an impact on the h^+ transport coming from the Si bulk to the surface depending on the NP surface coverage and/or distribution. However, the closer one gets to the surface, the less pronounced this effect is. The lateral VB modulations in Figure 11d-e taken at 1 and 10 nm depth show that at the surface very close to the NP (1nm depth), the barrier height is the same for 1, 3 or 15 NPs (Figure 11d). The small barrier between NPs is observed when the section is taken at a depth of 10 nm (Figure 11e. Between the “under NPs” and "under Electrolyte" zones, it actually changes from ~ 0.2 eV for one and three NPs, to 0.08 eV for fifteen NPs. This implies that h^+ coming from bulk Si, would indeed experience a lower energy barrier at the Si/Electrolyte regions between NPs than at the outer Si/Electrolyte regions, and thus could more easily etch between NPs (shallow delocalized etching). This observation may support the shallow etching observed during Cu deposition. However, given the blocking nature of the NP/Si junction for a metal with W_m = 4.73 eV (Figure 9c), the h^+ injected from the NP cannot reach the bulk. Therefore, these simulations do not justify the shallow delocalized etching that we observe during Cu deposition. Even if the presence of a high Cu NP density over the entire Si surface can affect the VB energy modulation, the effect is not sufficient to justify the experimental results. For example, the etching of moderately p-doped Si substrate with Ag NP is very localized [20,51], in contrast to what is observed with Cu. Thus, we can conclude that the delocalized etching observed in the cross section in Figure 2 is actually an apparent delocalized etching, most likely due to a very high surface coverage, or some another chemically specific process not considered in our model.

Regarding CuPd, a striking observation is the presence of craters formed around the NPs in the case of NO_3^-, with relatively large unetched areas around them. Between Cu_0Pd_{100} and $Cu_{50}Pd_{50}$, the delocalization of the etching around the NPs (*i.e.* the crater size) increases with the Cu fraction. Taking into account the above simulations, we assume that the presence of Cu makes the Si/metal junction more ohmic than with Pd alone. We have proposed that Pd is

actually present in the form of PdH_x, with a reduced work function, which tends to give a Schottky contact with Si (rather than ohmic). The etching is thus localized under the PdH_x NPs. For CuPd/Si, the resulting more ohmic contact could lead to delocalized etching of Si under the polarization induced by NO_3^-. The higher the Cu content, the less hydrided Pd would be and the more delocalized the etching. The W_m value determined for $Pd_{50}Cu_{50}$ by KP-AFM is 4.85 eV (see the SI), lower than the 4.92 eV measured for pure Pd, but higher than the 4.73 eV estimated for PdH_x. This may indeed justify a more ohmic contact in the case of CuPd compared to PdH_x.

Sequential deposition results in a different morphology of the metal coating. When a small amount of Cu is deposited first (1 min), Pd forms Pd-rich NPs in the second step. Conversely, with a large amount of Cu on the surface (5 min), Pd deposition leads to a homogeneous distribution of Pd, resulting in a porous, film-like coating. The higher Cu coverage in the latter case provides a homogeneous surface, while Cu NPs surrounded by Si (in the former case) forces localized Pd deposition. Compared to Cu_{50}/Pd_{50} obtained after (1 min - 1 min), the lower-than-expected amount of Pd after (5 min - 5 min), Cu_{65}/Pd_{35}, is probably due to the fact that Cu covers most of the surface after 5 min of deposition, which reduces the Pd deposition rate since the Si surface is less accessible to the electrolyte (limited anodic dissolution rate).

4 Conclusion

A novel method for bimetallic NP deposition on Si based on MACE has been presented. The Si sample is immersed in an HF solution containing both metal cations for simultaneous electroless deposition or in two HF solutions, one with each metal cation, for sequential deposition. $CuSO_4$, $PdNO_3$ and $PdCl_2$ have been used as metal salt precursors.

SEM-EDX characterizations have revealed that, in the case of simultaneous deposition, isolated CuPd NPs are preferentially formed as solid solutions, with a homogeneous composition that can be finely controlled by the concentration ratio of Cu^{2+} and Pd^{2+}. Sequential deposition results in NPs with separated Cu/Pd phases. XPS analysis has shown that the electrocatalytic properties (i.e. d-band center) of the bimetallic NPs can be tuned by modifying the bimetallic composition and the deposition parameters. Electrochemical responses have evidenced similarities between the CuPd and Pd deposition mechanism (similar OCP trends) *vs.* Cu. Finally, band bending simulations at selected polarization values have helped to interpret the localization observed for the Si etching around NPs as a function of the metal work function.

The above studies have led us to some conclusions: (1) during simultaneous deposition Pd centers act as Cu sinks, due to its higher noble character and the diffusion gradients generated, (2) the Si/Pd junction generated during MACE seems to be of Schottky type (Wm lower than expected). This may be due to the formation of PdH_x rather than Pd, and it is accentuated in the presence of oxidant counterions like NO_3^-, (3) in the presence of Cu, the Pd/Si junction becomes more ohmic, with delocalized etching around the NPs. These conclusions are only a first step toward the understanding of the mechanisms involved, and require further investigation.

The proposed method proceeds with Si dissolution, sometimes resulting in high surface roughness or dissolution craters, which can be modulated by the choice of metals (i.e. oxidizing power of the counterions and/or metal work functions). However, this method has many advantages for bimetallic deposition on Si: it is simple and easily scalable, it allows a good control of the alloy stoichiometry, as well as obtaining solid solutions or phase-separated bimetallics at the NP scale. These are key features to control the activity and selectivity of bimetallic systems for photo/electrocatalytic processes. Finally, it can be generalized to all metals that can be deposited by MACE of Si (Pt, Pd, Au, Ag and Cu, among others).

5 References

[1] V. Bertagna, F. Rouelle, G. Revel, M. Chemla, Electrochemical and Radiochemical Study of Copper Contamination Mechanism from HF Solutions onto Silicon Substrates, J. Electrochem. Soc. 144 (1997) 4175–4182. https://doi.org/10.1149/1.1838162.

[2] M. Chemla, T. Homma, V. Bertagna, R. Erre, N. Kubo, T. Osaka, Survey of the metal nucleation processes on silicon surfaces in fluoride solutions: from dilute HF to concentrated NH4F solutions, Journal of Electroanalytical Chemistry. 559 (2003) 111–123. https://doi.org/10.1016/S0022-0728(02)01280-9.

[3] K.-Q. Peng, Y.-J. Yan, S.-P. Gao, J. Zhu, Synthesis of large-area silicon nanowire arrays via self-assembling nanoelectrochemistry, Advanced Materials. 14 (2002) 1164.

[4] S. Yae, N. Nasu, K. Matsumoto, T. Hagihara, N. Fukumuro, H. Matsuda, Nucleation behavior in electroless displacement deposition of metals on silicon from hydrofluoric acid solutions, Electrochimica Acta. 53 (2007) 35–41. https://doi.org/10.1016/j.electacta.2007.04.058.

[5] C. Chartier, S. Bastide, C. Lévy-Clément, Metal-assisted chemical etching of silicon in HF–H2O2, Electrochimica Acta. 53 (2008) 5509–5516. https://doi.org/10.1016/j.electacta.2008.03.009.

[6] K. Tsujino, M. Matsumura, Boring Deep Cylindrical Nanoholes in Silicon Using Silver Nanoparticles as a Catalyst, Advanced Materials. 17 (2005) 1045–1047. https://doi.org/10.1002/adma.200401681.

[7] P. Gorostiza, J. Servat, J.R. Morante, F. Sanz, First stages of platinum electroless deposition on silicon (100) from hydrogen fluoride solutions studied by AFM, Thin Solid Films. 275 (1996) 12–17. https://doi.org/10.1016/0040-6090(95)07009-5.

[8] V. Lehmann, The electrochemistry of silicon: instrumentation, science, materials and applications, Wiley-VCH, Weinheim, 2002.

[9] X.G. Zhang, Electrochemistry of Silicon and its Oxide, Springer, 2001. http://link.springer.com/content/pdf/10.1007/b100331.pdf (accessed June 6, 2016).

[10] A.A. Ensafi, M. Jafari-Asl, B. Rezaei, Graphene/nano-porous silicon and graphene/bimetallic silicon nanostructures (Pt–M, M: Pd, Ru, Rh), efficient electrocatalysts for the hydrogen evolution reaction, Phys. Chem. Chem. Phys. 17 (2015) 23770–23782. https://doi.org/10.1039/C5CP04361A.

[11] M. Shepida, O. Kuntyi, G. Zozulya, E. Kaniukov, Deposition of palladium nanoparticles on the silicon surface via galvanic replacement in DMSO, Appl Nanosci. 10 (2020) 2563–2568. https://doi.org/10.1007/s13204-019-01018-0.

[12] M. Metzler, A. Thorwart, S. Zeller, T. Diemant, R.J. Behm, T. Jacob, Electroless deposition of Au/Pt/Pd nanoparticles on p-Si(111) for the light-induced hydrogen evolution reaction, Catalysis Today. 244 (2015) 3–9. https://doi.org/10.1016/j.cattod.2014.10.026.

[13] L. Chen, J.M. Chabu, Y. Liu, Bimetallic AgM (M = Pt, Pd, Au) nanostructures: synthesis and applications for surface-enhanced Raman scattering, RSC Adv. 3 (2013) 4391. https://doi.org/10.1039/c3ra23137b.

[14] B.T. Meshesha, N. Barrabés, J. Llorca, A. Dafinov, F. Medina, K. Föttinger, PdCu alloy nanoparticles on alumina as selective catalysts for trichloroethylene hydrodechlorination to ethylene, Applied Catalysis A: General. 453 (2013) 130–141. https://doi.org/10.1016/j.apcata.2012.12.019.

[15] J.K. Mathiesen, E.D. Bøjesen, J.K. Pedersen, E.T.S. Kjær, M. Juelsholt, S. Cooper, J. Quinson, A.S. Anker, G. Cutts, D.S. Keeble, M.S. Thomsen, J. Rossmeisl, K.M.Ø. Jensen, Breaking with the Principles of Coreduction to Form Stoichiometric Intermetallic PdCu Nanoparticles, Small Methods. 6 (2022) 2200420. https://doi.org/10.1002/smtd.202200420.

[16] A. Liu, H. Geng, C. Xu, H. Qiu, A three-dimensional hierarchical nanoporous PdCu alloy for enhanced electrocatalysis and biosensing, Analytica Chimica Acta. 703 (2011) 172–178. https://doi.org/10.1016/j.aca.2011.07.039.

[17] L. Lu, X. Sun, J. Ma, D. Yang, H. Wu, B. Zhang, J. Zhang, B. Han, Highly Efficient Electroreduction of CO_2 to Methanol on Palladium–Copper Bimetallic Aerogels, Angewandte Chemie International Edition. 57 (2018) 14149–14153. https://doi.org/10.1002/anie.201808964.

[18] T. Takashima, T. Suzuki, H. Irie, Electrochemical carbon dioxide reduction on copper-modified palladium nanoparticles synthesized by underpotential deposition, Electrochimica Acta. 229 (2017) 415–421. https://doi.org/10.1016/j.electacta.2017.01.171.

[19] E. Torralba, N. Blanchard, C. Cachet-Vivier, D. Muller-Bouvet, J. González, S. Bastide, Electrochemical study of carbon dioxide reduction at copper–palladium nanoparticles: Influence of the bimetallic composition in the CO poisoning tolerance, Electrochim. Acta. 354 (2020) 136739. https://doi.org/10.1016/j.electacta.2020.136739.

[20] E. Pinna, S. Le Gall, E. Torralba, G. Mula, C. Cachet-Vivier, S. Bastide, Mesopore Formation and Silicon Surface Nanostructuration by Metal-Assisted Chemical Etching With Silver Nanoparticles, Front. Chem. 8 (2020) 1–13. https://doi.org/10.3389/fchem.2020.00658.

[21] E. Torralba, S. Le Gall, R. Lachaume, V. Magnin, J. Harari, M. Halbwax, J.-P. Vilcot, C. Cachet-Vivier, S. Bastide, Tunable Surface Structuration of Silicon by Metal Assisted Chemical Etching with Pt Nanoparticles under Electrochemical Bias, ACS Appl. Mater. Interfaces. 8 (2016) 31375–31384. https://doi.org/10.1021/acsami.6b09036.

[22] J. Cichoszewski, M. Reuter, F. Schwerdt, J.H. Werner, Role of catalyst concentration on metal assisted chemical etching of silicon, Electrochimica Acta. 109 (2013) 333–339. https://doi.org/10.1016/j.electacta.2013.07.079.

[23] K. Tamarov, R. Kiviluoto, J.D. Swanson, B.A. Unger, A.T. Ernst, M. Aindow, J. Riikonen, V.-P. Lehto, K.W. Kolasinski, Low-Load Metal-Assisted Catalytic Etching Produces Scalable Porosity in Si Powders, ACS Appl. Mater. Interfaces. 12 (2020) 48969–48981. https://doi.org/10.1021/acsami.0c13980.

[24] J.F. Moulder, Handbook of X-ray Photoelectron Spectroscopy: A Reference Book of Standard Spectra for Identification and Interpretation of XPS Data, Physical Electronics Division, Perkin-Elmer Corporation, 1992.

[25] R. Feng, Q. Zhu, M. Chu, S. Jia, J. Zhai, H. Wu, P. Wu, B. Han, Electrodeposited Cu–Pd bimetallic catalysts for the selective electroreduction of CO_2 to ethylene, Green Chem. 22 (2020) 7560–7565. https://doi.org/10.1039/D0GC03051A.

[26] X. Jiang, N. Koizumi, X. Guo, C. Song, Bimetallic Pd–Cu catalysts for selective CO_2 hydrogenation to methanol, Applied Catalysis B: Environmental. 170–171 (2015) 173–185. https://doi.org/10.1016/j.apcatb.2015.01.010.

[27] S. Hu, S. Ha, L. Scudiero, Temperature dependence study of Pd–Cu supported bimetallic films by photoelectron spectroscopy and cyclic voltammetry, Electrochimica Acta. 105 (2013) 362–370. https://doi.org/10.1016/j.electacta.2013.05.012.

[28] W.J. Wang, S. Hwang, T. Kim, S. Ha, L. Scudiero, Study of carbon supported CuPd alloy nanoparticles with Pd-rich surface for the electrochemical formate oxidation and CO_2 reduction, Electrochimica Acta. 387 (2021) 138531. https://doi.org/10.1016/j.electacta.2021.138531.

[29] T. Hofmann, T.H. Yu, M. Folse, L. Weinhardt, M. Bär, Y. Zhang, B.V. Merinov, D.J. Myers, W.A. Goddard, C. Heske, Using Photoelectron Spectroscopy and Quantum Mechanics to Determine d-Band Energies of Metals for Catalytic Applications, J. Phys. Chem. C. 116 (2012) 24016–24026. https://doi.org/10.1021/jp303276z.

[30] C. Wei, Y. Sun, G.G. Scherer, A.C. Fisher, M. Sherburne, J.W. Ager, Z.J. Xu, Surface Composition Dependent Ligand Effect in Tuning the Activity of Nickel–Copper Bimetallic Electrocatalysts toward Hydrogen Evolution in Alkaline, J. Am. Chem. Soc. 142 (2020) 7765–7775. https://doi.org/10.1021/jacs.9b12005.

[31] B.S. Mun, M. Watanabe, M. Rossi, V. Stamenkovic, N.M. Markovic, P.N. Ross, A study of electronic structures of Pt_3M (M=Ti,V,Cr,Fe,Co,Ni) polycrystalline alloys with valence-band photoemission spectroscopy, J. Chem. Phys. 123 (2005) 204717. https://doi.org/10.1063/1.2126662.

[32] M.T. Gorzkowski, A. Lewera, Probing the Limits of d-Band Center Theory: Electronic and Electrocatalytic Properties of Pd-Shell–Pt-Core Nanoparticles, J. Phys. Chem. C. 119 (2015) 18389–18395. https://doi.org/10.1021/acs.jpcc.5b05302.

[33] T. Gunji, H. Ochiai, T. Ohira, Y. Liu, Y. Nakajima, F. Matsumoto, Preparation of Various Pd-Based Alloys for Electrocatalytic CO_2 Reduction Reaction-Selectivity Depending on Secondary Elements, Chem. Mater. 32 (2020) 6855–6863. https://doi.org/10.1021/acs.chemmater.0c01137.

[34] S. Chatterjee, C. Griego, J.L. Hart, Y. Li, M.L. Taheri, J. Keith, J.D. Snyder, Free Standing Nanoporous Palladium Alloys as CO Poisoning Tolerant Electrocatalysts for the Electrochemical Reduction of CO_2 to Formate, ACS Catal. 9 (2019) 5290–5301. https://doi.org/10.1021/acscatal.9b00330.

[35] Z. Yin, D. Gao, S. Yao, B. Zhao, F. Cai, L. Lin, P. Tang, P. Zhai, G. Wang, D. Ma, X. Bao, Highly selective palladium-copper bimetallic electrocatalysts for the electrochemical reduction of CO_2 to CO, Nano Energy. 27 (2016) 35–43. https://doi.org/10.1016/j.nanoen.2016.06.035.

[36] J.H. Lee, S. Kattel, Z. Jiang, Z. Xie, S. Yao, B.M. Tackett, W. Xu, N.S. Marinkovic, J.G. Chen, Tuning the activity and selectivity of electroreduction of CO2 to synthesis gas using bimetallic catalysts, Nat Commun. 10 (2019) 3724. https://doi.org/10.1038/s41467-019-11352-0.

[37] D.R. Turner, On the Mechanism of Chemically Etching Germanium and Silicon, J. Electrochem. Soc. 107 (1960) 810–816. https://doi.org/10.1149/1.2427519.

[38] J.J. Kelly, X.H. Xia, C.M.A. Ashruf, P.J. French, Galvanic cell formation: a review of approaches to silicon etching for sensor fabrication, IEEE Sensors Journal. 1 (2001) 127-. https://doi.org/10.1109/JSEN.2001.936930.

[39] M. Chemla, T. Homma, V. Bertagna, R. Erre, N. Kubo, T. Osaka, Survey of the metal nucleation processes on silicon surfaces in fluoride solutions: from dilute HF to concentrated NH4F solutions, Journal of Electroanalytical Chemistry. 559 (2003) 111–123. https://doi.org/10.1016/S0022-0728(02)01280-9.

[40] D. Pletcher, F.C. Walsh, Industrial Electrochemistry, Springer, 1990. https://link.springer.com/book/9780412304101.

[41] S. Schönekerl, J. Acker, The Role of the Molecular Hydrogen Formation in the Process of Metal-Ion Reduction on Multicrystalline Silicon in a Hydrofluoric Acid Matrix, Nanomaterials. 11 (2021) 982. https://doi.org/10.3390/nano11040982.

[42] W. Liu, S. Zhang, N. Li, J. Zheng, S. An, G. Li, Influence of Dealloying Solution on the Microstructure of Monolithic Nanoporous Copper through Chemical Dealloying of Al 30 at.% Cu Alloy, Int. J. Electrochem. Sci. 7 (2012).

[43] S.J. MacHardy, L.J.J. Janssen, The diffusion coefficient of Cu(II) ions in sulfuric acid–aqueous and methanesulfonic acid–methanol solutions, Journal of Applied Electrochemistry. 34 (2004) 169–174. https://doi.org/10.1023/B:JACH.0000009956.75577.ef.

[44] M. Uemoto, Measurements of Diffusion Coefficients of Aqua- and Chloro-Complexes of Palladium(II) and Mercury(II) in Aqueous Solutions, Inorganic Reaction Mechanisms. 2 (1999) 155–159.

[45] H.B. Michaelson, The work function of the elements and its periodicity, Journal of Applied Physics. 48 (1977) 4729–4733. https://doi.org/10.1063/1.323539.

[46] H.B. Michaelson, The work function of the elements and its periodicity, Journal of Applied Physics. 48 (2008) 4729–4733. https://doi.org/10.1063/1.323539.

[47] S. Halas, T. Durakiewicz, Work functions of elements expressed in terms of the Fermi energy and the density of free electrons, J. Phys.: Condens. Matter. 10 (1998) 10815. https://doi.org/10.1088/0953-8984/10/48/005.

[48] J. Hölzl, F.K. Schulte, Work function of metals, in: J. Hölzl, F.K. Schulte, H. Wagner (Eds.), Solid Surface Physics, Springer, Berlin, Heidelberg, 1979: pp. 1–150. https://doi.org/10.1007/BFb0048919.

[49] S. Yae, M. Tashiro, M. Abe, N. Fukumuro, H. Matsuda, High Catalytic Activity of Palladium for Metal-Enhanced HF Etching of Silicon, Journal of The Electrochemical Society. 157 (2010) D90. https://doi.org/10.1149/1.3264643.

[50] G. Behzadi pour, L. Fekri aval, Highly sensitive work function hydrogen gas sensor based on Pd NPs/SiO_2/Si structure at room temperature, Results in Physics. 7 (2017) 1993–1999. https://doi.org/10.1016/j.rinp.2017.06.026.

[51] S. Bastide, E. Torralba, M. Halbwax, E. Mpogui, C. Cachet-Vivier, V. Magnin, J. Harari, D. Yarekha, J.-P. Vilcot, 3D Patterning of Si by Contact Etching With Nanoporous Metals, Frontiers in Chemistry. 7 (2019) 13. https://doi.org/10.3389/fchem.2019.00256.

CRediT authorship contribution statement

E. Torralba: Conceptualization, Formal analysis, Investigation, Funding acquisition, Supervision, Writing - original draft; Writing - review & editing. **H. Chaliyawala**: Data curation, Investigation. **S. Le Gall**: Data curation, Formal analysis, Conceptualization, Investigation, Writing - review & editing, **E. Chopard**: Data curation, Investigation, **Z. Ait Rahou:** Data curation, Investigation, **D. Muller-Bouvet:** Data curation, Investigation. **C. Cachet-Vivier:** Supervision, **S. Bastide:** Conceptualization, Investigation, Funding acquisition, Supervision, Validation, Writing - original draft; Writing - review & editing.

Declaration of Competing Interest

The authors declare that they have no known competing financial interests or personal relationships that could have appeared to influence the work reported in this paper.

Data availability

The data used will be made available upon request.

Acknowledgements

The authors acknowledge P. Dubot, K. Bah and R. Pires for their technical assistance with the XPS and SEM-EDX measurements (Spectroscopy and Microscopy facilities of the East-Paris Institute of Chemistry and Materials). We also acknowledge José Alvarez for the KP-AFM measurements (AFM Platform of the Laboratory of Electrical Engineering of Paris) E. Torralba thanks A. Torralba-Peñalver for his help with the d-band center calculations, and J. Gonzalez and E. Laborda, for their guidance with the electrochemical mixed potential theory**.** Finally, the authors acknowledge the support of the Centre National de la Recherche Scientifique (CNRS) and University of Paris-Est Creteil (UPEC) for providing the central facilities to carry out this work.

Funding

This work was supported by the French National Research Agency (ANR JCJC SIROCCO 2022-2024) and the I-Site Project Future (Exploratory project EVOLVE 2021-2022, Gustave Eiffel University). H. Chaliyawala acknowledges Paris-East Creteil University (UPEC) for his postdoctoral fellowship (2020-2021).